

DISSERTATION

DESIGNING NOVEL RADIO-FREQUENCY COILS FOR HIGH FIELD AND ULTRA-HIGH FIELD  
MAGNETIC RESONANCE IMAGING

Submitted by

Pranav Shrikant Athalye

Department of Electrical and Computer Engineering

In partial fulfillment of the requirements

For the Degree of Doctor of Philosophy

Colorado State University

Fort Collins, Colorado

Fall 2021

Doctoral Committee:

Advisor: Branislav Notaroš

Milan Ilić

Ali Pezeshki

Thomas Johnson

Copyright by Pranav Shrikant Athalye 2021

All Rights Reserved

## ABSTRACT

### DESIGNING NOVEL RADIO-FREQUENCY COILS FOR HIGH FIELD AND ULTRA-HIGH FIELD MAGNETIC RESONANCE IMAGING

High field and ultra-high field magnetic resonance imaging is the upcoming technology in the field of magnetic resonance imaging. This has created the need for designing of new radio frequency (RF) coils. Here are presented several of these novel RF coils include multifilar helical antenna coils for 3-T, 4.7-T, 7-T and 10.5-T NMR scanners, slotted-waveguide array coils for 7-T, inverted microstrip array coil for 7-T along with other methods to improve the efficiency and homogeneity of the RF field. The coils were simulated using commercial electromagnetic solvers including WIPL-D and ANSYS-HFSS, and some were also measured experimentally. The results for  $B_1^+$  efficiency are compared with state-of-art coils. These novel coils exhibit high  $B_1^+$  efficiency, strong right-hand polarization, good field homogeneity with an acceptable level of SAR. Details of numerical methods for the simulations of the coils has also been discussed. Ongoing work and future plans have also been presented.

## ACKNOWLEDGMENTS

I would like to start by thanking all the gods, ancestors, and teachers. I would like to thank my advisor Dr. Branislav Notaroš for his guidance, encouragement, and immense patience. I have grown as a research student and as a professional under his guidance. I would like to thank Dr. Milan Ilić for his continual guidance and help. I would also like to thank my other committee members Dr. Ali Pezeshki and Dr. Thomas Johnson. I would like to especially thank Olivera Notaroš for lending help from time to time. I would like to acknowledge Sanja Manić and Nada Šekeljić for helping get accustomed to being a research student. I would also like to acknowledge Ana Manić, Elene Chobanyan, Cameron Kleinkort, Aaron Smull, Nabeel Moin, Cameron Key, Jake Harmon, Blake Troksa, Stephen Kasdorf, and Jeremiah Corrado for their support. And most importantly, I would like to thank my loving family whose efforts and prayers have made be able to pursue my dreams.

## TABLE OF CONTENTS

ABSTRACT.....	ii
ACKNOWLEDGMENTS .....	iii
INTRODUCTION .....	1
1 HELICAL-ANTENNA RF COIL FOR 3-T MRI.....	4
1.1 Introduction.....	4
1.2 Methods.....	5
1.3 Results Analysis, and Discussion.....	8
1.4 Conclusion .....	18
2 HELICAL-ANTENNA RF COIL FOR 7-T AND 10.5-T MRI.....	20
2.1 Introduction.....	20
2.2 Methods.....	21
2.3 Results and Discussion .....	25
2.4 Conclusion .....	35
3 SLOTTED-WAVEGUIDE ARRAY COIL .....	36
3.1 Introduction.....	36
3.2 Materials and Methods.....	36
3.3 Results and Discussion .....	40
3.4 Conclusion .....	41
4 IMPROVING RF FIELD EFFICIENCY AND HOMOGENEITY USING DIELECTRIC LOADING .....	42
4.1 Dielectric Loading in Traveling Wave MRI.....	42
4.2 Using Dielectric Loading as Buffer .....	46
4.3 Dielectric Loading as Dielectric Lenses .....	49
5 MODELING OF MRI RF COILS USING COMMERCIALY AVAILABLE ELECTROMAGNETIC SOLVERS .....	51
5.1 Introduction.....	51
5.2 FEM and MOM Modeling.....	51
5.3 Results and Discussion .....	53
6 ONGOING AND FUTURE WORK.....	56
6.1 Helical Antenna RF Coil for 4.7-T MRI.....	56
6.2 Inverted Microstrip Array RF Coil for 7-T MRI .....	57
REFERENCES .....	61
PUBLICATIONS.....	70

## INTRODUCTION

While the terminology largely varies, high field (HF) or very high field and ultra-high field (UHF) magnetic resonance (MR) scanners are usually referred to the main polarizing static magnetic field values of  $3 \text{ T} \leq B_0 < 7 \text{ T}$  ( $127.8 \text{ MHz} \leq f_0 < 300 \text{ MHz}$ ) and  $B_0 \geq 7 \text{ T}$  ( $f_0 \geq 300 \text{ MHz}$ ), respectively, with the low-field systems and mid-field systems being those with  $B_0 < 3 \text{ T}$ . Here,  $f_0$  is the so-called Larmor frequency, which is proportional to  $B_0$  [1]–[4]. The main area of engineering research in advancing MR scanners is improving radio-frequency (RF) coils (exciters) and RF-excitation magnetic fields,  $B_1$ , more precisely, right-hand circularly polarized (RCP) RF magnetic fields, usually denoted as  $B_1^+$ . This is the area of focus of this proposed research, aimed at introducing, developing, and establishing novel RF volume exciters and dramatically advancing RF coil designs for HF and UHF MR. Our proposed approach and novel method for excitation of RF  $B_1^+$  field is based largely on subject-loaded multi-channel RF volume coils for HF and UHF MRI. This includes multifilar helical antenna coil for 3-T, 4.7-T, 7-T and 10.5-T MR scanners, and a slotted-waveguide array coil for 7-T MR scanner. We also propose methods involving dielectric loading, facilitating traveling wave MR imaging. The proposed research is aimed to, longer term, significantly advance both state-of-the-art clinical HF MRI scanners and next generation UHF MRI systems. The matrices along which these proposed methods may be shown to provide improvement are: field efficiency, field uniformity (homogeneity), axial ratio (of polarization), specific absorption rate (SAR).

Whereas most MR imaging (MRI) machines in human medical practice operate at 1.5 T and lower  $B_0$ , state-of-the-art clinical MRI scanners are 3-T systems ( $B_0 = 3 \text{ T}$ ), i.e., HF magnets, with MRI bores measuring typically 60 cm in diameter, which allows full-body human subjects. However, 3-T scanners are uncommon in hospitals, where 1.5-T scanners are common. 3-T MRI are not common due to higher costs, field inhomogeneity issues, and specific absorption rate (SAR) constraints. Furthermore, cutting-edge research centers in neuroscience and/or MRI favor UHF scanners because higher  $B_0$  values

yield higher signal-to-noise ratio (SNR), that can be traded for higher spatial resolution (hundreds of microns), as well as higher parallel imaging performances allowing for higher acquisition acceleration factor [5]–[10]. Successful results with recent HF and UHF MR technology [5], [6], [11], [12], especially in the human brain, have convinced several tens of top-level biomedical research centers throughout the world to acquire 7-T scanners; promising human brain MRI data have been obtained at 9.4-T [13]–[16], and even higher fields (such as 10.5 T) human scanners are being built or installed.

Optimization and utilization of all the advantages of HF and UHF MRI requires addressing very difficult challenges, dominated by RF excitation spatial heterogeneity and RF induced local tissue heating (SAR, found as  $\sigma|\mathbf{E}|^2/\rho$ , with  $\sigma$  standing for the conductivity and  $\rho$  for the mass density of the tissue, and  $\mathbf{E}$  for the electric field intensity vector). Dramatic improvements in image quality have been obtained using RF coil arrays with multi-channel RF transmit technology [17]–[21]; however, RF coil design for human HF/UHF scanners remains an area of intense development [7], [12], [22], [23], especially regarding the most challenging targets, namely those requiring torso RF excitation [24]–[27], also known as “body imaging”. A fundamental issue at HF/UHF, with increasing Larmor frequency (e.g., 200 MHz at 4.7 T and 300 MHz at 7 T), comes from the reduced RF wavelengths, down to the order of or smaller than the size of the imaged samples, resulting in a fairly complex mix of near-field and far-field RF behaviors. This yields highly nonuniform  $B_1$  field distribution, an issue quickly identified as one of the main challenges to develop HF and UHF MRI technology in humans [28]–[30]. Moreover, while the MR scanner at clinical field strength of  $B_0 = 1.5$  T is considered to be a developed technology, there still are a number of major engineering challenges associated with the design of an optimal RF coil even at the HF strength of  $B_0 = 3$  T.

Overall, the principal desired objectives for the development and design of HF and UHF RF coils and  $\mathbf{B}_1$  fields inside an MRI bore loaded with a human or a phantom can be summarized as follows. First, there should be a strong coupling of the field with a subject and deep field penetration into the tissues. Second, a good circular polarization (CP) of the transverse components of  $\mathbf{B}_1$  in the subject should be

achieved. The more circularly polarized  $\mathbf{B}_1$  field, the higher the transmit efficiency that results into higher SNR. Third, a high spatial uniformity of the transverse  $\mathbf{B}_1^+$  field along the MRI bore, large field of view (FOV), and as uniform as possible RCP transverse field,  $\mathbf{B}_1^+$ , elsewhere in the subject are desired. Transverse  $\mathbf{B}_1^+$  field uniformity is directly related to the resulting MRI image quality. The last requirement is that the local as well as averaged total SAR values must be, for the given total input RF power of the system, well below the acceptable and allowable prescribed SAR levels, to prevent any potential health hazards.

# 1 HELICAL-ANTENNA RF COIL FOR 3-T MRI

## 1.1 Introduction

The goal of this research is to, design, simulate, and evaluate a novel method for excitation of RF  $B_1$  field in state-of-the-art high-field MRI systems, with  $B_0 = 3$  T and Larmor frequency of  $f_0 = 127.8$  MHz, using a subject-loaded quadrifilar helical antenna as a RF coil. [31]. Full-wave electromagnetic simulations of 3-T MRI systems with phantom-loaded helical antennas show efficient coupling and deep field penetration into the phantoms, high  $B_1^+/B_1^-$  ratio and spatial uniformity throughout the phantoms, large FOV, good transmit efficiency, and low SAR levels at every point in the phantom. Overall, our novel RF coil provides substantially better  $B_1^+$  field uniformity and much larger FOV than any of the previously reported results in literature. Moreover, it shows great potential for whole-body imaging [32] at 3 T.

Design, analysis, characterization, and evaluation of the proposed quadrifilar helical exciter, when situated in a 3-T MRI bore and loaded with different phantoms, is performed by extensive numerical simulations using a higher-order full-wave computational electromagnetics (CEM) [33] technique based on the method of moments in the surface integral equation formulation [34]. Whereas only MRI experiments will ultimately validate the properties and confirm the practical relevance of the new coil, simulation results presented in this study are rigorously checked and evaluated with all relevant numerical and modeling aspects, as well as thoroughly verified and validated by comparison with results using two well-established commercial full-wave CEM codes.

A novel subject-loaded quadrifilar helical-antenna RF coil for 3-T MRI is proposed to meet the goal. A proof-of-concept four-channel helical RF body coil, with high  $B_1^+$  field uniformity and large FOV, at 3 T is presented. In the presented examples, the proposed coil is compared with 3-T MRI scanners utilizing existing state-of-the-art RF coil designs, in the cases where the reported results for these designs provide sufficient information for a meaningful comparison. The proposed system differs in

concept to the existing birdcage design. Our results indicate that the new design shows an increase in performance and promises to complement the currently used solutions for 3-T MRI scanners and provides an avenue for further exploration.

## 1.2 Methods

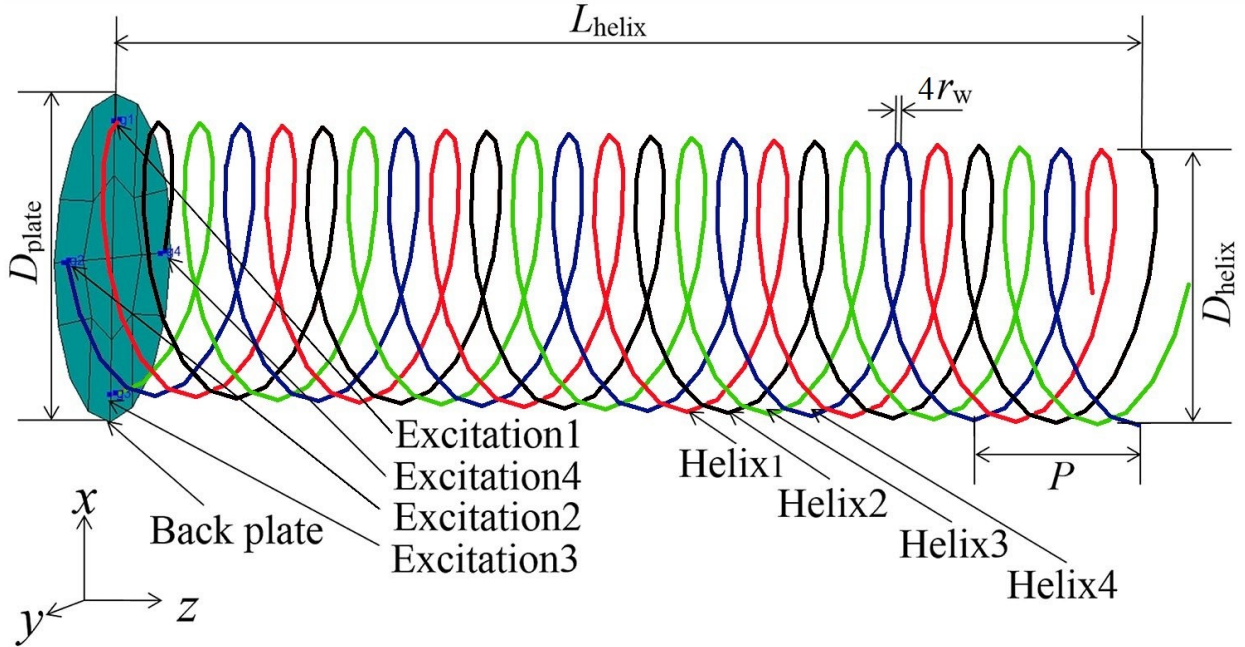


**Fig. 1.1.** Quadrifilar helical antenna in free space. The antenna consists of four helices (Helices 1–4) fed by four delta-function generators (Excitations 1–4) with complex RMS voltages  $V + j0$ ,  $0 - jV$ ,  $-V + j0$ , and  $0 + jV$ , respectively.

A helical antenna represents a metallic wire wound uniformly and periodically with  $N$  wire turns and a pitch  $P$  about an imaginary (or dielectric) cylinder of diameter  $D_{\text{helix}}$  and length  $L_{\text{helix}} = NP$  [35], shown as Helix 1 (a single filament) in Fig. 1.1. The pitch  $P$  relates to the pitch angle,  $\alpha$ , as  $P = C_{\text{helix}} \tan \alpha$ , where  $C_{\text{helix}} = \pi D_{\text{helix}}$  is the helix circumference. The antenna is fed at one wire end against a circular back plate, acting as a ground plane, i.e., the input power is supplied at a lumped excitation port (a delta-function generator [34]) between the wire end and the plate. For practical MRI RF excitation at 3 T, we specifically propose a four-channel helical RF coil – with high  $B_1^+$  field uniformity and large FOV. The proposed coil is a quadrifilar helical antenna, where four helices (Helices 1–4 in Fig. 1.1) are

wound coaxially and fed in time-phase quadrature, i.e., by  $90^\circ$  out of phase with respect to each other (with complex voltages of delta-function generators equaling  $V + j0$ ,  $0 - jV$ ,  $-V + j0$ , and  $0 + jV$ , respectively, where  $j = \sqrt{-1}$  is the imaginary unit), against the common back plate, so their currents flow along the wires in time-phase quadrature.

Design of the proposed quadrifilar helical exciters, as well as analysis of the RF electromagnetic field in 3-T MRI bores generated by the exciters, are performed using a full-wave CEM technique based on the method of moments (MoM) in conjunction with the surface integral equation (SIE) approach [33], implemented in a numerically higher-order fashion [33]. In this technique, all material (metallic and dielectric) surfaces in the structure are modeled using generalized parametric quadrilateral patches. All metallic wires are modeled by means of straight wire segments. Electric and magnetic equivalent surface currents over elements (quadrilateral patches and wire segments) are modeled by polynomial vector basis functions. The SIEs based on boundary conditions for electric and magnetic field vectors are solved employing the Galerkin method [34]. In addition, the results obtained by the higher-order MoM-SIE technique are verified and validated by comparison with results using two well-established commercial full-wave CEM codes, a MoM code WIPL-D [36] and a finite element method (FEM) code ANSYS HFSS [37].

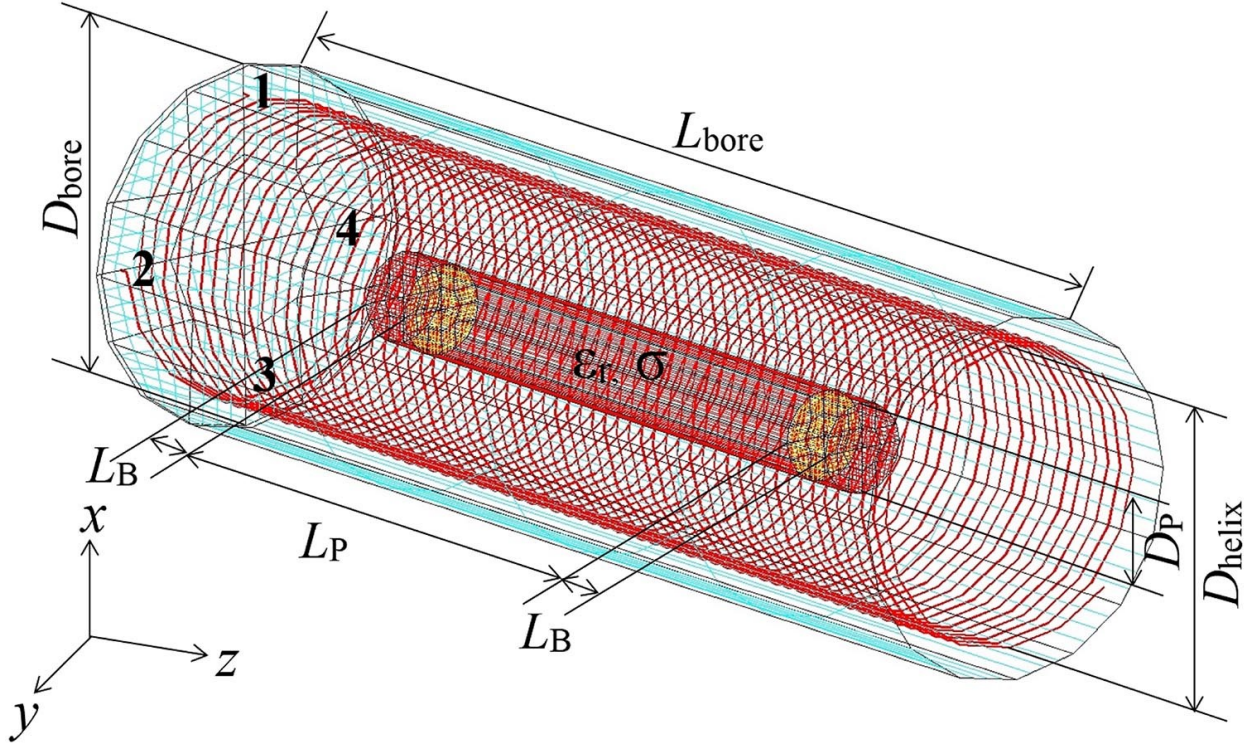


**Fig. 1.2.** Application of the novel method for excitation of RF  $B_1$  field in high-field ( $B_0 = 3$  T) MRI systems: 3-T MRI metallic bore with an RF body coil in the form of a phantom-loaded quadrifilar helical antenna (Fig. 1.1) at an operating frequency of  $f_0 = 127.8$  MHz, with the accepted powers at the four excitation ports (Excitations 1–4), i.e., time-average powers delivered to the ports, being  $P_{a1}$ ,  $P_{a2}$ ,  $P_{a3}$ , and  $P_{a4}$ , respectively. The cylindrical phantom (of length  $L_P$ ) is terminated at both ends with small cylindrical buffers (of length  $L_B$ ) made of the same material.

To demonstrate the novel method for RF excitation using a subject-loaded helical antenna as an RF exciter – at 3 T, Fig. 1.2 shows a 3-T system with a bore in the form of a metallic cylinder of diameter  $D_{\text{bore}} = 60$  cm and length  $L_{\text{bore}} = 200$  cm (simplified model of a clinical scanner). The bore is coaxially and centrally loaded with a phantom in the form of a cylinder of diameter  $D_p$  and length  $L_p$  filled with a homogeneous lossy dielectric of relative permittivity  $\epsilon_r$ , conductivity  $\sigma$ , and relative permeability  $\mu_r = 1$ . Note that in MRI related experiments and simulations, a phantom is a container of an arbitrary (but usually simple) shape, most commonly a cylindrical bottle, that is filled with a fluid resembling relative permittivity (dielectric constant) and conductivity parameters of human tissues and has NMR active species such as hydrogen molecules, e.g., saline water or deionized (DI) water. In order to prevent abrupt field changes and wave reflections at the ends of the phantom due to abrupt material discontinuities

between the phantom medium and surrounding air, the phantom is terminated at each end with a cylindrical buffer of length  $L_B$  and the same diameter,  $D_B = D_P$ , made of the same material as the phantom (Fig. 1.2).

The RF magnetic field  $\mathbf{B}_1$  in the bore and in the phantom is excited by a phantom-loaded quadrifilar helical antenna, of diameter  $D_{\text{helix}}$  and length  $L_{\text{helix}}$ , with the pitch and wire radius of each of the four helices being  $P$  and  $r_w$ , respectively, placed coaxially with respect to the bore and the phantom and fed as in Fig. 1, against the back plate of diameter  $D_{\text{plate}}$ , at an operating frequency of  $f_0 = 127.8$  MHz. In addition to a solid back-plate, a designs with a hollow back-plate (metallic ring) of outer and inner diameters  $D_{\text{plate1}}$  and  $D_{\text{plate2}}$ , respectively, was also evaluated. In clinical applications, a solid back-plate closing off one end of the MRI bore may be impractical, and the hollow one may be preferred in order to provide more comfort to the patient and better access to the bore. Additionally, strong surface eddy currents induced on a continuous plate may generate RF noise, which, if the plate is close to the subject, may adversely affect the SNR of the image; these currents may even cause strong mechanical vibration of the plate and loud acoustic noise during the scan, due to the changing magnetic gradient.

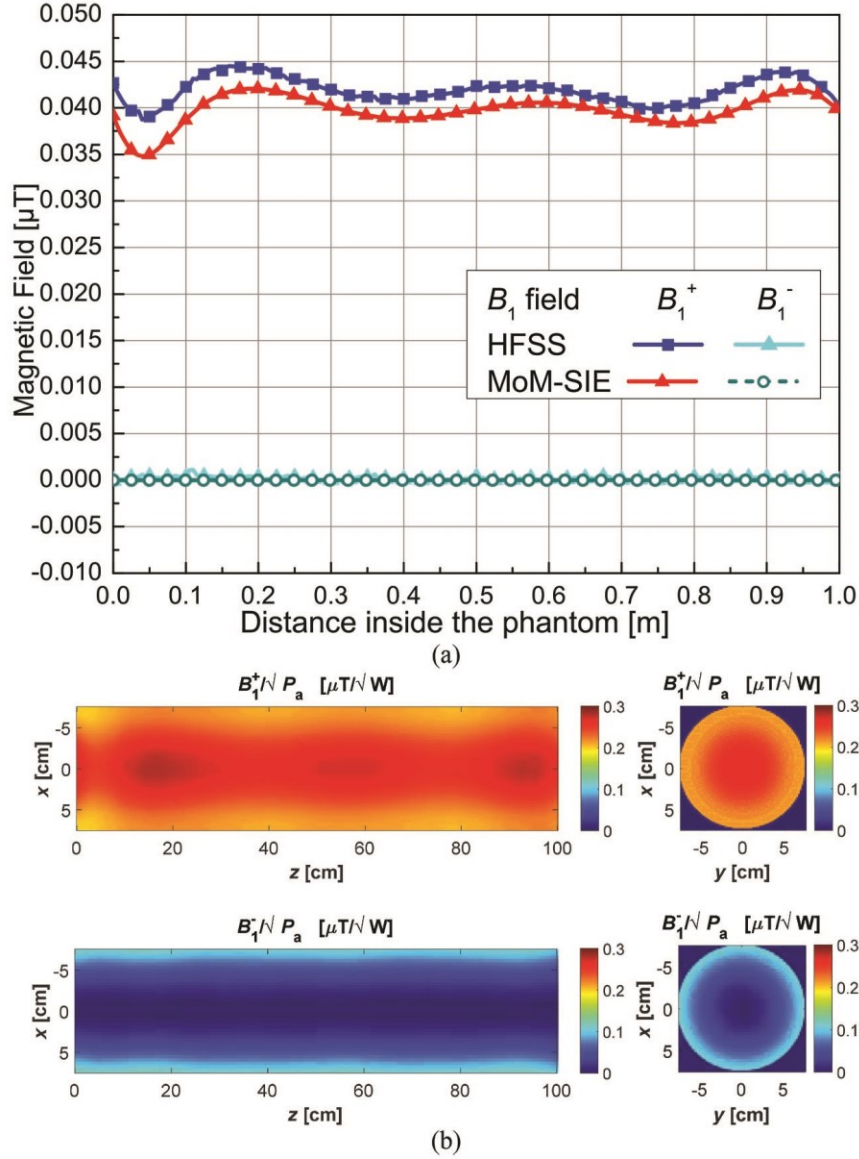
In terms of further improvements of the designs, parameters of the helical antenna, e.g., the helix pitch, diameter, and length, can be varied and optimized for even better performance of the 3-T MRI system. Different feeding patterns and terminations of helices are also possible, as well as tapering of the windings. Multifilar antennas can also be designed and implemented to utilize parallel imaging [38].

### 1.3 Results Analysis, and Discussion

As the first example, we consider a 3-T MRI system in Fig. 1.2 ( $D_{\text{bore}} = 60$  cm,  $L_{\text{bore}} = 200$  cm) with a quadrifilar helical RF body coil exciter in Fig. 1.2 with dimensions, material properties and accepted power as given in Table 1.1 and  $f_0 = 127.8$  MHz.

Table 1.1.

$D_{\text{helix}}$ (cm)	$L_{\text{helix}}$ (cm)	$P$ (cm)	$r_w$ (cm)	$D_{\text{plate}}$ (cm)	$D_P$ (cm)	$D_B$ (cm)	$L_P$ (cm)	$L_B$ (cm)	$\epsilon_r$	$\sigma$ (s/m)	$P_{a1-4}$ (mW)
50	200	12.8	0.1	60	15	15	100	10	81	0.6	4.7



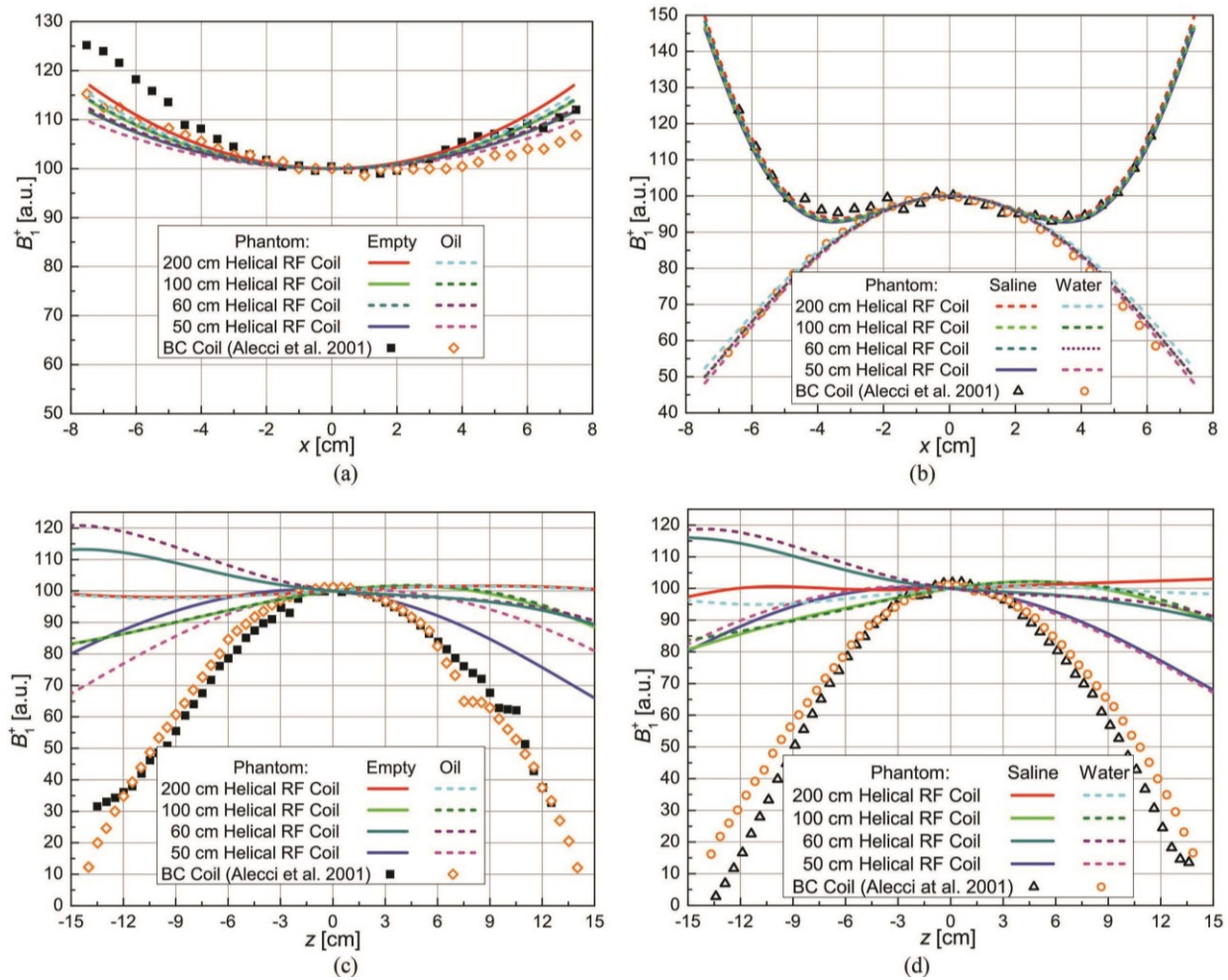
**Fig. 1.3.** (a) 1-D distribution of the RCP component of the transverse RF magnetic field,  $B_1^+$ , and the LCP component,  $B_1^-$ , inside the saline-water phantom in the 3-T MRI system in Fig. 1.2 (parameters given in the text) along its axis ( $z$ -axis): comparison of the results obtained using the MoM-SIE technique and those by ANSYS HFSS commercial code. (b) 2-D RCP (transmit efficiency) and LCP normalized-field maps in the coronal ( $y = 0$ ) and axial ( $z = 50$  cm, in the middle of the phantom) cross sections of the phantom computed by ANSYS-HFSS. The maximum efficiency should be compared with the efficiencies in [39-47].

Fig. 1.3(a) shows the one-dimensional (1-D) distribution of the RCP component of the transverse RF magnetic field,  $B_1^+$ , and the left-hand CP (LCP) component,  $B_1^-$ , along the axis of the phantom ( $z$ -axis) in Fig. 1.2. Note that it is customary in MRI literature to refer to  $B$  as simply the magnetic field, whereas in electromagnetics  $B$  generally stands for the magnetic flux density or magnetic induction, in the units of T (tesla), and the magnetic field intensity (strength), in the units of A/m, is denoted by  $H$  [48]. In free space and nonmagnetic media, the relationship between the magnetic flux density and field intensity vectors is  $\mathbf{B} = \mu_0 \mathbf{H}$  ( $\mu_0$  is permeability of free space,  $\mu_0 = 4\pi \cdot 10^{-7}$  H/m). Note also that what we show is the RMS value of  $B$ , that is, the RMS magnitude of the complex vector  $\mathbf{B}$ . We observe from the figure that  $B_1^-$  is practically vanishing and that a perfect (i.e. 1)  $B_1^+/B_1^-$  ratio and a perfectly RCP  $B_1^+$  field are achieved along the  $z$ -axis inside the saline-water phantom placed inside the quadrifilar helical RF body coil in the 3-T MRI system in Fig. 1.2. We also observe an almost perfect spatial uniformity (less than  $\pm 10\%$  variation) of the transverse  $B_1^+$  field along the  $z$ -axis.

In addition, we validate, in Fig. 1.3(a), the MoM-SIE model and results by comparing them with those obtained by ANSYS HFSS, and an excellent qualitative agreement between the two sets of results (mean deviation of 4.5%) is observed. Validation is important given that the two solution approaches used are completely different, both conceptually and numerically; the MoM-SIE is a surface modeling technique that solves boundary integral equations for currents, while HFSS is a volumetric modeling technique that solves partial differential equations for fields. The agreement is not perfect primarily due to a difference in the helix models – in the HFSS solution, we use thin rectangular strip elements of widths  $w_s$ , whereas in the MoM-SIE solution, the helices are modeled with cylindrical thin wire elements of radii  $r_w = w_s/4$ . Important details of MoM-SIE and FEM (HFSS) full-wave electromagnetic modeling of RF fields in MRI applications that enable rigorous analyses and cross-validation of the solutions in characterizations of RF coils are presented in [49].

Shown in Fig. 1.3(b) are two-dimensional (2-D) field maps of  $B_1^+$  and  $B_1^-$  components of  $\mathbf{B}_1$  in the coronal/sagittal and axial cross sections of the phantom in Fig. 1.2, where we observe a very small  $B_1^-$

when compared to  $B_1^+$  and therefore an almost perfect RCP  $B_1^+$  field throughout the entire phantom, as well as an almost perfect (less than  $\pm 20\%$  variation) spatial uniformity of the transverse  $B_1^+$  field throughout the phantom. More specifically, Fig. 1.3(b) shows the transmit efficiency evaluated as  $B_1^+/\sqrt{P_a}$ , where  $P_a = P_{a1} + P_{a2} + P_{a3} + P_{a4}$  is the total accepted power for the coil, as well as the corresponding normalization of the LCP field,  $B_1^-/\sqrt{P_a}$ . The maximum efficiency in Fig. 1.3(b) is comparable in value with those reported for various coils and phantoms at 3 T, as well as 7 T, in [39-47].



**Fig. 1.4.**  $B_1^+$  field in the transversal direction ( $y = z = 0$ ) inside the 3-T MRI scanner in Fig. 1.2 (parameters given in the text) when the bore is (a) empty or loaded with a vegetable oil phantom—case (A) and (b) loaded with a saline solution phantom—case (B) or a water phantom—case (C): comparison of the MoM-SIE numerical results for the quadrifilar helical RF coil—of four different lengths—with experimental results for the 16-element quadrature birdcage (BC) coil from [50]. (c)–(d) The same as in (a)–(b) but for  $B_1^+$  field in the longitudinal direction ( $x = y = 0$ ) inside the 3-T MRI scanner.

**Table 1.2.**

$D_{\text{helix}}$ (cm)	$P$ (cm)	$r_w$ (cm)	$D_{\text{plate}}$ (cm)	$D_P$ (cm)	$D_B$ (cm)	$L_P$ (cm)	$L_B$ (cm)
58	12.8	0.1	60	15	15	38	10

In the next example, we further analyze the magnetic field  $B_1$  uniformity of the system in Fig. 1.2. The helical antenna RF coil and phantom dimensions are as given in Table 1.2 ( $D_{\text{bore}} = 60$  cm,  $L_{\text{bore}} = 200$  cm,  $f_0 = 127.8$  MHz). The phantom was filled with three different dielectrics [50] which cover the dielectric properties of a range of biological tissue, one at a time: (A) vegetable oil ( $\epsilon_r = 2.9$ ,  $\sigma = 0$ ), (B) saline water ( $\epsilon_r = 78$ ,  $\sigma = 1.67$  S/m), and (C) water ( $\epsilon_r = 74$ ,  $\sigma = 0$ ), and the buffers in Fig. 1.2 are made of the same material as in cases (A)–(C), respectively. Moreover, we consider four different designs of the quadrifilar helical RF coil, with: (i)  $L_{\text{helix1}} = 200$  cm and  $D_{\text{plate}} = 60$  cm (solid back-plate, like in the previous example), (ii)  $L_{\text{helix2}} = 100$  cm, a hollow back-plate (metallic ring) with  $D_{\text{plate1}} = 59$  cm and  $D_{\text{plate2}} = 50$  cm, and the helical structure being positioned in the bore such that the back plate is located at a distance of 30 cm from the bore opening, (iii)  $L_{\text{helix3}} = 60$  cm, the hollow back-plate as in (ii), and the structure position such that the back plate is 71 cm away from the bore opening, and (iv)  $L_{\text{helix3}} = 50$  cm and the hollow back-plate at 73.5 cm from the bore opening.

**Table 1.3.** Maximum percentage variation in the  $B_1^+$  field with respect to the field at the center of the field of view i.e.  $\delta B_{\text{max}}$  in the longitudinal direction ( $x = y = 0$ ) inside the 3-T MRI scanner for various RF coils and phantoms.

	Empty ( $\epsilon_r = 1$ , $\sigma = 0$ S/m)	Veg Oil ( $\epsilon_r = 2.9$ , $\sigma = 0$ S/m),	Saline ( $\epsilon_r = 78$ , $\sigma = 1.67$ S/m)	Water ( $\epsilon_r = 74$ , $\sigma = 0$ S/m)
200 cm Helical RF Antenna	1.84%	2.14%	3.94%	3.22%
100 cm Helical RF Antenna	17.43%	16.74%	19.98%	16.31%
60 cm Helical RF Antenna	13.24%	20.87%	16.33%	18.63%
50 cm Helical RF Antenna	34.45%	33.29%	31.91%	31.35%
BC Coil (Alecci et al. 2001)	69.11%	88.52%	84.84%	98.73%

We compare the MoM-SIE numerical results for the described helical exciters with experimental results for the 16-element quadrature birdcage coil (of diameter 27.8 cm and length 21 cm) from [50].

Fig. 1.4 shows the 1-D field distributions in the transversal direction (axial cross section) along the  $x$ -axis ( $y = z = 0$ ) and the longitudinal direction (coronal/sagittal cross section) along the  $z$ -axis ( $x = y = 0$ ), respectively, for the empty bore and phantoms (A)–(C). All results are normalized with respect to  $B_1$  at the center of the phantom, as suggested in [50], and given in “arbitrary units” (a.u.). Namely, we are not able to perform comparison in absolute (non-normalized) values and physical units because the results in [50] are given in a.u.

From Fig. 1.4(a)–(b) and Table 1.3, we conclude that the numerical results for the proposed quadrifilar helical RF coil show a comparable field uniformity in the transversal direction as the birdcage coil measurements in [50], for all four phantom cases and all four helical coil lengths. Moreover, based on Fig. 1.4(c)–(d), we conclude that the helical-antenna exciters with all four lengths yield remarkable improvements in the field uniformity in the longitudinal direction in all four phantom cases as compared to the birdcage coil results in [50], with the maximum field variation with respect to the mean value of the signal,  $\delta B_{\max}$ , for  $L_{\text{helix}} = 200$  cm being less than 4%. Specifically, the computed maximum field variations for empty bore and phantoms (A), (B), and (C) are  $\delta B_{\max} = 1.84\%$ ,  $2.14\%$ ,  $3.94\%$ , and  $3.22\%$ , respectively. The maximum field variation when the bore is empty, for instance, reported in [50] is  $\delta B_{\max} = 10\%$  within 9 cm inside the phantom, whereas in our case,  $\delta B_{\max}$  is approximately five times lower and is computed along the whole length of the phantom ( $L_P = 38$  cm). In other words, with the quadrifilar helical RF coil ( $L_{\text{helix}} = 200$  cm), the usable FOV is increased approximately 4.22 times, and similarly for the other three coil lengths.

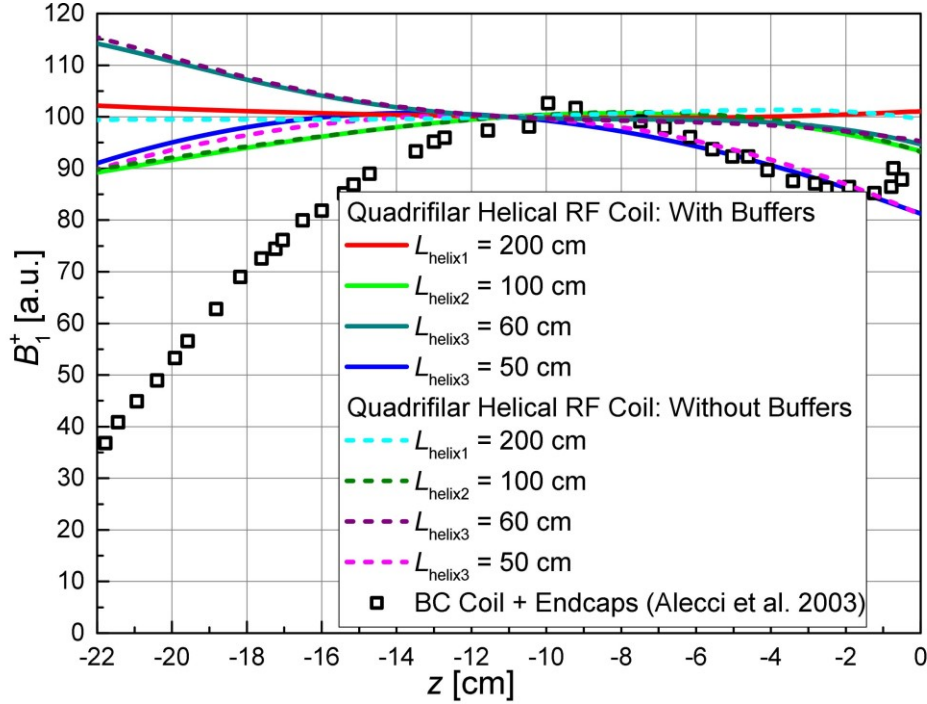


**Fig. 1.5.**  $B_1^+$  field in the longitudinal direction ( $x = y = 0$ ) inside the 3-T MRI scanner in Fig. 1.2 (parameters given in the text) with the vegetable oil phantom: comparison of the MoM-SIE results—for four different lengths of the quadrifilar helical RF coil and for the phantom with and without buffers (Fig. 1.2)—with the experimental results obtained with an improved birdcage coil [51].

We next compare our results for the vegetable oil phantom, case (A), in the longitudinal plane with the results obtained with an improved birdcage coil hardware using detached endcaps as described in [50]. The phantom, with  $D_P = D_B = 17$  cm and  $L_P = 26$  cm (all structure parameters except  $L_{\text{helix}}$ ,  $D_P$ ,  $D_B$ , and  $L_P$  are as in Fig. 1.4), is coaxially placed with respect to the bore in all four designs (i)–(iv) of the helical RF coil, and we consider two configurations: the phantom with and without dielectric buffers (in Fig. 1.2), respectively.

**Table 1.4.** Maximum percentage variation in the  $B_1^+$  field with respect to the field at the center of the field of view i.e.  $\delta B_{\text{max}}$  in the longitudinal direction ( $x = y = 0$ ) inside the 3-T MRI scanner for various RF coils.

	$L_{\text{helix1}} = 200$ cm	$L_{\text{helix1}} = 100$ cm	$L_{\text{helix1}} = 60$ cm	$L_{\text{helix1}} = 50$ cm
Quadrifilar Helical RF Coil: With Buffers	2.31%	11.06%	14.48%	19.14%
Quadrifilar Helical RF Coil: Without Buffers	1.42%	10.87%	15.03%	19.15%
BC Coil + Endcaps (Alecci et al. 2003)	63.67%			

As shown in Fig. 1.5 (again, the results are normalized and given in a.u. to match [51]) and Table 1.4, the results obtained with the shorter quadrifilar helical RF coil [designs (ii)–(iv)] are still considerably more uniform than the results in [51], even with the reported 85% improvement of the  $B_1$  field at the service end of the birdcage with respect to that at the coil’s center when detached endcaps are used [51]. We also observe that the results for the phantom without buffer terminations are almost equally good. With the  $\delta B_{\max}$  improving from 63.67% to as little as 1.42%, it can be concluded that the quadrifilar helical RF coil provides a significant improvement when compared to the birdcage coil [50], [51] in the longitudinal direction (and even when the helical exciter is short).

**Table 1.5.**

$D_{\text{helix}}$ (cm)	$P$ (cm)	$r_w$ (cm)	$D_{\text{plate}}$ (cm)	$D_P$ (cm)	$D_B$ (cm)	$L_P$ (cm)	$L_B$ (cm)	$\epsilon_r$	$\sigma$ (s/m)	$P_{\text{a1-4}}$ (mW)
58	12.8	0.1	60	10	10	60	10	69.062	1.505	6.62

Next, we consider a 3-T MRI system in Fig. 1.2 with  $D_{\text{bore}} = 60$  cm,  $L_{\text{bore}} = 200$  cm,  $f_0 = 127.8$  MHz, and helical RF coil and phantom (from [52]) parameters as shown in Table 1.5. Fig. 1.6 shows 2-D  $B_1^+$  and  $B_1^-$  field maps in the coronal/sagittal and axial cross sections. As expected and observed from the figure, and based on the previous examples, the quadrifilar helical RF body coil design provides an almost perfect spatial uniformity ( $\delta B_{\max} = 12.3\%$ ) of the transverse  $B_1^+$  field and an almost perfect  $B_1^+/B_1^-$  ratio i.e. close to 1 throughout the phantom. In terms of  $B_1^+$  field uniformity, our design yields a notable improvement and outperforms the parallel-plate waveguide design (two 25 cm wide, 60 cm long, and 6  $\mu\text{m}$  thick aluminum strips, mounted on an acrylic cylinder, 30 cm in diameter and 60 cm long) in conjunction with the embedded birdcage coil (66 cm in diameter and 68 cm long, with 16 rungs driven in quadrature) inside the 3-T MRI system described and shown in Fig. 1(a) in [52]. For 2-D field comparison, see the results for the 3-T MRI system shown in Fig. 2 in [52].

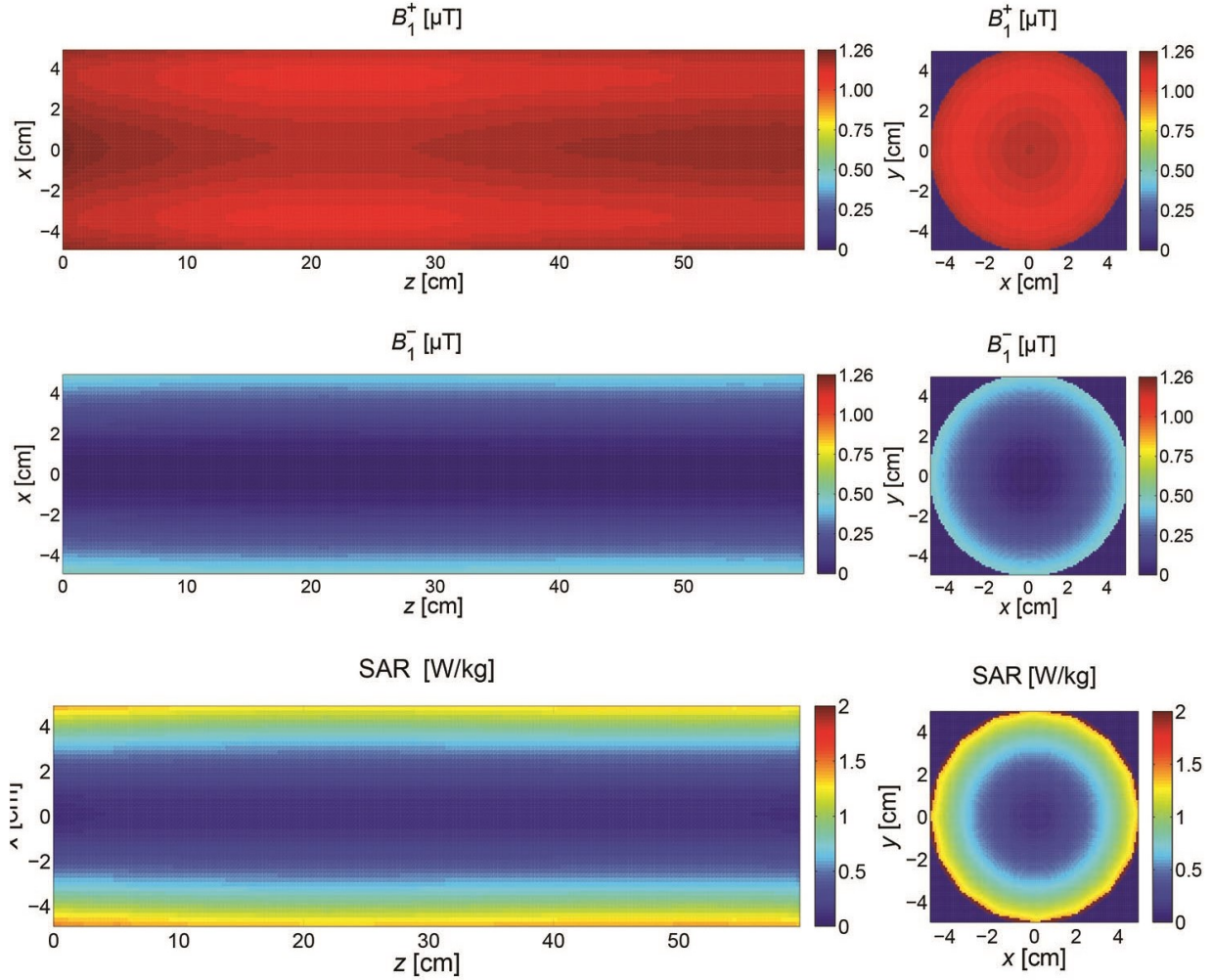


**Fig. 1.6.** MoM-SIE 2-D field maps of  $B_1^+$  and  $B_1^-$  fields and local SAR in the coronal ( $y = 0$ ) and axial ( $z = 30$  cm, in the middle of the phantom) cross sections of the phantom in the 3-T MRI system in Fig. 1.2 (parameters given in the text). The  $B_1^+$  and  $B_1^-$  results were compared with computed, using COMSOL Multiphysics, field maps in Fig. 2 in [52] for the parallel-plate waveguide design in conjunction with the embedded birdcage coil. The SAR results were compared with the SAR values reported in Fig. 4(c) in [52].

In addition, shown in Fig. 1.6 is also the distribution of the local SAR in the coronal and central axial cross sections of the phantom. It can be observed from the figure that the SAR, for the given typical or maximal total input RF power of the MRI system, would be below the allowable prescribed SAR level at every point of the phantom. The maximum SAR level we observe is 1.5 W/kg, which is within the permissible SAR range. These results are in a good agreement with the SAR range reported in Fig. 4(c) in [52].

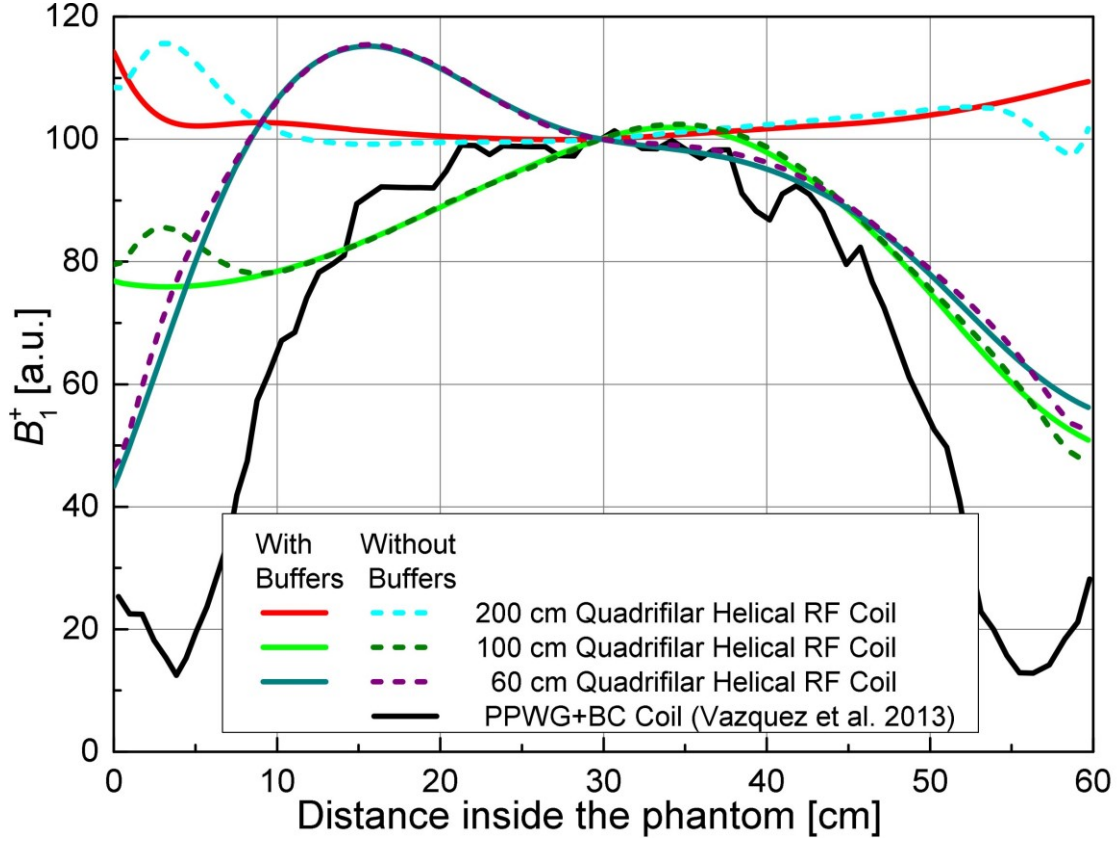


**Fig. 1.7.**  $B_1^+$  field inside the phantom along its longitudinal axis in the 3-T MRI system in Fig. 1.2 (system parameters as in Fig. 1.6): comparison of the MoM-SIE results for the quadrifilar helical RF body coil of three different lengths and the phantom with and without buffers (Fig. 1.2) with COMSOL Multiphysics results for the parallel-plate waveguide (PPWG) + birdcage (BC) coil [53] (note that the graph is directly traced from Fig. 3 in [52], where it looks different due to using a different scale; it is also qualitatively verified with the inset in Fig. 3 in [53])

**Table 1.6.** Maximum percentage variation in the  $B_1^+$  field with respect to the field at the center of the field of view i.e.  $\delta B_{\max}$  in the longitudinal direction ( $x = y = 0$ ) inside the 3-T MRI scanner for various RF coils.

	$L_{\text{helix1}} = 200$ cm	$L_{\text{helix1}} = 100$ cm	$L_{\text{helix1}} = 60$ cm
Quadrifilar Helical RF Coil: With Buffers	14.58%	47.76%	56.41%
Quadrifilar Helical RF Coil: Without Buffers	16.82%	54.07%	53.36%
PPWG + BC Coil (Vazquez et al. 2013)	87.49%		

In Fig. 1.7 and Table 1.6, we compare for uniformity the 1-D field distribution (normalized to the field level at the center of the phantom) for the quadrifilar helical-antenna RF body coil of three different lengths ( $L_{\text{helix}} = 200$  cm, 100 cm, and 60 cm) with that from [52], obtained using commercial FEM code COMSOL Multiphysics V. 3.2. Here, all results are normalized with respect to  $B_1$  at the center of the

phantom and given in “arbitrary units” (a.u.) because there is no information on the power in [52], so it is impossible to perform comparison in absolute values. We observe from the figure that the helical RF coil with  $L_{\text{helix}} = 200$  cm provides almost constant field along the phantom axis (in the longitudinal direction), as well as that the results for  $L_{\text{helix}} = 200$  cm, 100 cm, and 60 cm, whether the dielectric buffers are used at the ends of the phantom (Fig. 1.2) or not, are considerably more uniform than those from [52] for the same phantom.

#### 1.4 Conclusion

Here in this paper [31] we have proposed a novel method for excitation of RF  $B_1$  field in high-field ( $B_0 = 3$  T) MRI systems using a subject-loaded quadrifilar helical antenna as an RF coil. Analysis, characterization, evaluation, and demonstration of the proposed quadrifilar helical exciter when situated in a 3-T MRI bore and loaded with different phantoms have been performed by extensive numerical simulations using the higher-order method of moments in the surface integral equation formulation. The simulation results are fully representative and predictive of the performance of the proposed RF coil in the actual MRI bore.

The examples have shown that the helical-antenna exciter provides substantially better  $B_1^+$  field uniformity and much larger FOV than any of the reported numerical and experimental results in literature that enable comparison. It yields a remarkable improvement in the field uniformity in the longitudinal direction as compared to the reported results, with the maximum field variation with respect to the mean value of the signal for empty bore and various phantoms being many times lower. In addition, quadrifilar helical RF body coils of different lengths can, for instance, easily provide a highly uniform  $B_1^+$  field and excellent right-hand CP and  $B_1^+/B_1^-$  ratio within the lengths close to or exceeding practical FOV of 50 cm as defined by  $B_0$  field uniformity and gradient coil dimensions. Even the lengths of 100 cm can easily be covered, which might not be practical at the moment but is certainly interesting and noteworthy. The

transmit efficiencies evaluated as  $B_1^+/\sqrt{P_a}$ , with  $P_a$  standing for the total accepted power for the coil, are comparable with those reported for various coils and phantoms at 3 T, as well as 7 T. The SAR distributions and local SAR values in the phantoms are in agreements with the SAR distributions and ranges reported for similar 3-T systems. The simulation results for the homogeneous human body phantom inside the quadrifilar helical RF body coil at 3 T have shown a good overall  $B_1$  field uniformity, circular polarization, and SAR levels throughout the phantom.

Our future work will include measurements and experimental testing of the novel coil in a 3-T MRI scanner. This may include human-phantom CEM studies including heterogeneous numerical phantoms, further quantitative comparative studies relative to the corresponding existing RF coils at 3 T, further improvements of the designs, as well as designs and demonstrations of helical-antenna RF coils at fields other than 3 T, namely, at ultra-high fields.

## 2 HELICAL-ANTENNA RF COIL FOR 7-T AND 10.5-T MRI

### 2.1 Introduction

Since its inception, MRI has operated in the long-wavelength (quasi-static) regime where radio-frequency (RF) wavelength is much larger than the imaged sample. With the advent of UHF-MR human imagers, however, given the high dielectric constant,  $\epsilon_r$ , of tissues, the excitation wavelength becomes on the order of, or smaller than, the imaged sample, resulting in a fairly complex mix of near-field and far-field RF behaviors. Namely, at  $B_0 = 7$  T, with  $\epsilon_r$  typically about 50–55 in biological samples at this Larmor frequency ( $\sim 300$  MHz), the RF wavelength inside tissues is about 14 cm or less. Owing to this short wavelength, complex RF phase modulation and interference phenomena, commonly observed at microwave and optical frequencies but traditionally negligible in MR experiments, are readily observed in tissues at UHF. In practice, biological tissues behave like lossy dielectrics, resulting in a complex superposition of multiple propagating mode excitations intermixed with RF penetration attenuation, yielding highly nonuniform excitation magnetic field ( $B_1$ ) distribution, an issue quickly identified as one of the main challenges to develop UHF-MR technology in humans [7], [10], [15], [29], [30], [54]-[57]. Whereas in MR scanners operating at 3 T or lower magnetic field, the RF exciter is almost exclusively in the form of a whole body birdcage coil [58], generating a homogeneous right-hand circularly polarized (CP) RF magnetic field, usually denoted as  $\mathbf{B}_1^+$ , using a volume RF coil at UHF, especially in the body, basically seems to be an impossible task. Notable attempts to generate a more uniform  $B_1^+$  field with a body coil at 7 T with a TEM body coil [24] were not successful. Twisting a birdcage volume coil structure towards a spiral shape [59] has been proposed to distribute RF phase through space; however this was for head RF excitation and only at 4 T, thus in this instance, RF interactions were still dominated by a near-field or quasi-static regime.

In this proposal based on our [60] we design, simulate, and experimentally test the helical antenna coil in 7 T and 10.5 T MRI.

## 2.2 Methods

It is well known that helical antennas in their axial mode in free space (unbounded air-filled space), radiate a circularly polarized (CP), e.g., right-hand CP (RCP), endfire beam, i.e., RCP electromagnetic wave, along and near the helix axis far away from the helix [61], [62]. In addition, the helical antenna is essentially a traveling wave (TW) antenna – the current along the wire of the antenna, when operating in free space, behaves like a traveling current wave (except in the regions close to the beginning and the end of the helical winding). The expectation is that the TW current of the helical antenna, when placed in the MRI bore as an RF exciter and loaded with a phantom or a subject that is being imaged, will produce – inside the phantom (subject) – an RF magnetic field  $B_1$  that is RCP and more spatially uniform than with other RF body coils, thereby further enabling large FOV ( $> 30$  cm) clinical applications at UHF. Note that in other UHF attempts that also used helix coils at 7 T, the imaged sample was placed outside of the coil, and thereby exposed to the abovementioned extremely low RF power efficiency [63], [64].

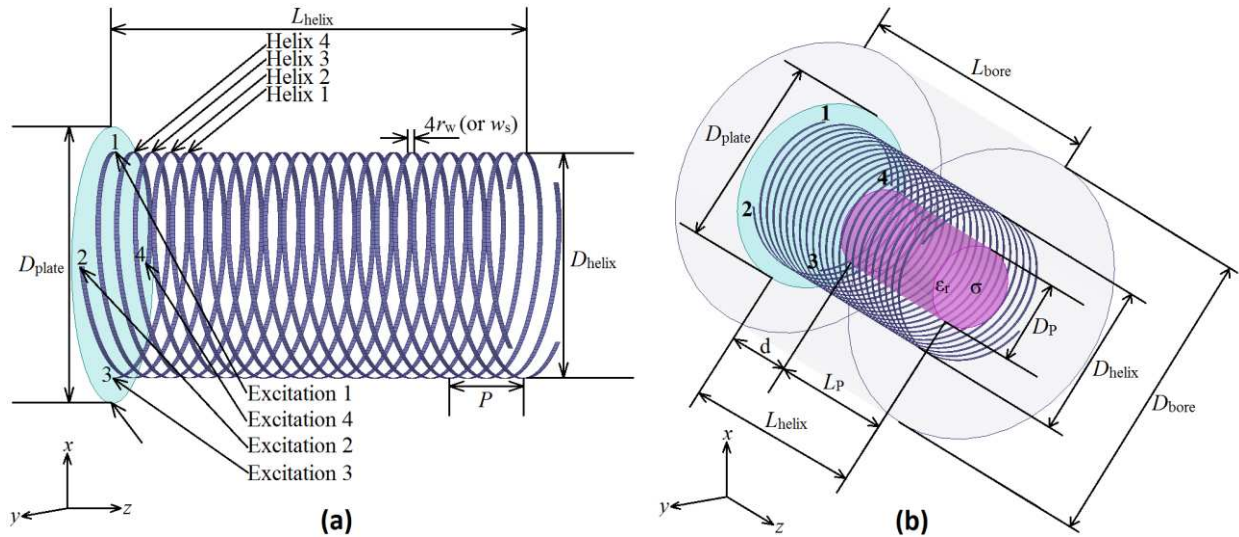


**Fig. 2.1.** (a) Sketch of a quadrifilar axial-mode helical antenna in free space. The antenna consists of four helices (Helices 1–4) fed by four generators (Excitations 1–4)  $90^\circ$  out of phase with respect to each other against the common back plate (complex RMS voltages of the generators are  $V + j0$ ,  $0 - jV$ ,  $-V + j0$ , and  $0 + jV$ , respectively, where  $j = \sqrt{-1}$  is the imaginary unit). (b) Higher order MoM-SIE simulation model of an UHF MRI metallic bore with a 4-channel RF volume coil in the form of a phantom-loaded helical antenna.

The basic structure of these helices seen in Fig. 2.1 is similar to that of the 3 T helix shown in Fig. 1.1 and Fig. 1.2 with some minor differences. The phantom is placed coaxially with the helical-antenna coil and the bore at a distance  $d$  from the back plate.

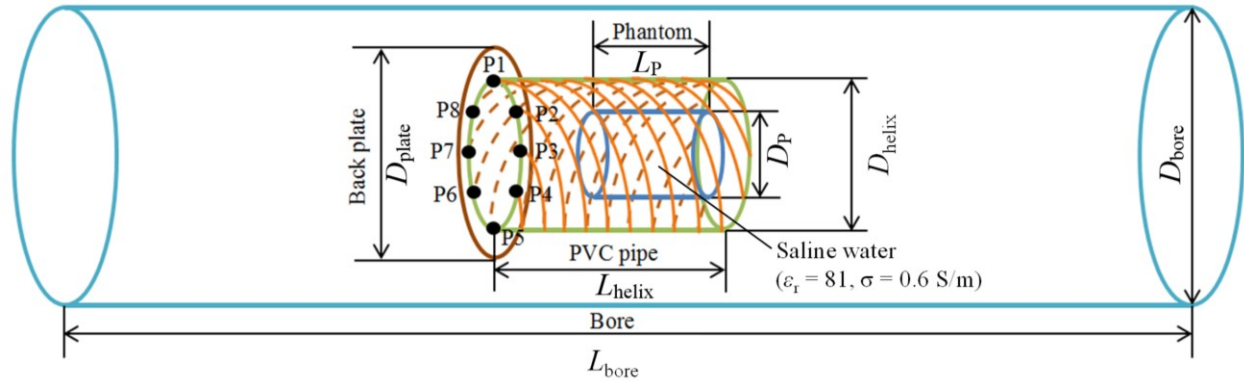


**Fig. 2.2.** Sketch of an octafilar (8-channel) phantom-loaded helical-antenna UHF (at 7 T and 10.5 T, respectively) MRI RF volume-coil prototype, with  $M$  helices wound coaxially and fed with  $360^\circ/M$  phase increments ( $M = 8$ ) against the common back plate (ports P1–P8), used in CMRR experiments; saline-water cylindrical “bottle” phantom is at the far end inside the coil.

We designed and fabricated several quadrifilar (4-channel) and octafilar (8-channel) helical-antenna RF coil prototypes at 7 T and 10.5 T, respectively, in the Electromagnetics Laboratory at Colorado State University, as depicted in Figs. 2.2 and 2.3. The prototypes are a 4-channel helical-antenna coil at 7 T ( $L_{\text{helix}} = 60$  cm,  $D_{\text{helix}} = 32$  cm), shown in Fig. 2.3(a), an 8-channel 7-T coil ( $L_{\text{helix}} = 65$  cm,  $D_{\text{helix}} = 32$  cm), Fig. 2.3(b), a 4-channel coil at 10.5 T ( $L_{\text{helix}} = 60$  cm,  $D_{\text{helix}} = 21$  cm), Fig. 2.3(c), and an 8-channel 10.5-T coil ( $L_{\text{helix}} = 60$  cm,  $D_{\text{helix}} = 21$  cm). In these prototypes, the individual helical spirals are narrow strips ( $w_s = 6$  mm) realized from a 35- $\mu\text{m}$  thick copper tape, and the weights are  $\sim 11.3$  kg and  $\sim 6.8$  kg for the 7-T and 10.5-T prototypes, respectively.

Another interesting feature of our designs is that in all helical-antenna RF coil prototypes we designed and built, the exciters are internally matched and do not need any matching circuits – in free space, outside of the MRI bore and prior to being loaded with a phantom or subject. This is done, at both 7 T and 10.5 T, by including specially designed matching plates at each of the four/eight helices [each plate is about a quarter/eighth of the helix circumference long and starts right after the respective

connector (excitation port) and ends right before the next port in a quadri/octafilar antenna arrangement], as shown in Fig. 3(d). Variation of widths and lengths of the matching plates together with fine tuning of coil wire (strip) lengths, is conducted to optimally match the coils internally, before further tuning the coil once placed in the scanner bore and loaded for MRI experiments. The return loss, measured in free space, is better than 10 dB for all ports, for all quadrifilar coils, and better than 8 dB for all ports, for all octafilar coils. Hence, the reflected power is only 10% or 15% or less in all cases. In addition, the coupling between the channels is below -10 dB for both quadrifilar and octafilar helical-antenna coils. In general, by tuning the matching at the ports, input VSWR (voltage standing wave ratio) can always be kept below 2 for quadrifilar helices and below 2.5 for octafilar helices.

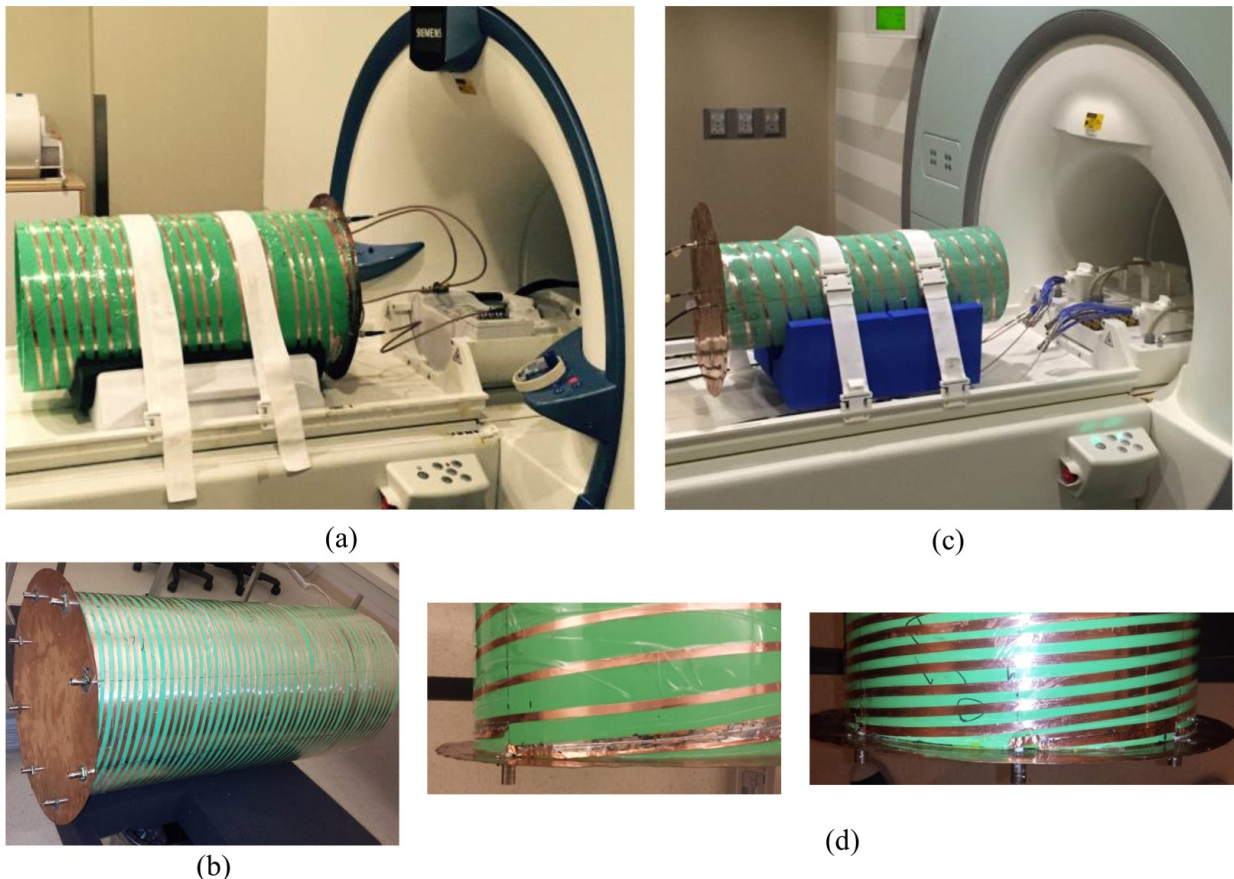


**Fig. 2.3.** (a) Multi-channel helical-antenna inner-volume RF coil prototypes during CMRR experiments: (a) 4-channel ( $M = 4$ ) 7-T, 300-MHz, prototype (Fig. 1), (b) 8-channel ( $M = 8$ ) 7-T, 300-MHz, prototype (Fig. 2), (c) 4-channel 10.5-T, 443-MHz, prototype (Fig. 1), and (d) specially designed matching plates at each of the four/eight helices of the 4-channel (left) and 8-channel (right) 7-T prototypes – internally matched antennas in free space.

The helical-antenna RF coil prototypes were tested, validated, and evaluated experimentally in 7-T and 10.5-T MR scanners at the Center for Magnetic Resonance Research (CMRR), University of Minnesota [see Figs. 2.3(a), 2.3(c), and 2.5(a)]. The MRI experiments were performed using phantoms in the form of a cylindrical “bottle” filled with saline water [see Fig. 2.5(a)], and using the phantom-loaded multi-channel helix coil as a transceiver (Tx and Rx simultaneously). Saline-water phantoms are standard phantoms used at the CMRR. Moreover, some of the examples from the literature, used here for comparison, also employ saline-water phantoms [50, 51]. The saline solution, although not an ideal substitute for human tissue, is an excellent medium widely used to observe the mode structures in UHF MRI. The electrical properties of the saline solution are such that they efficiently model the loss and small enough wavelengths arising from its high permittivity. In the saline solution, whose permittivity is higher than or equal to any other material tissue inside a human body, the wavelength is smaller than the wavelength in the human body, so it provides a worst-case scenario.

## 2.3 Results and Discussion

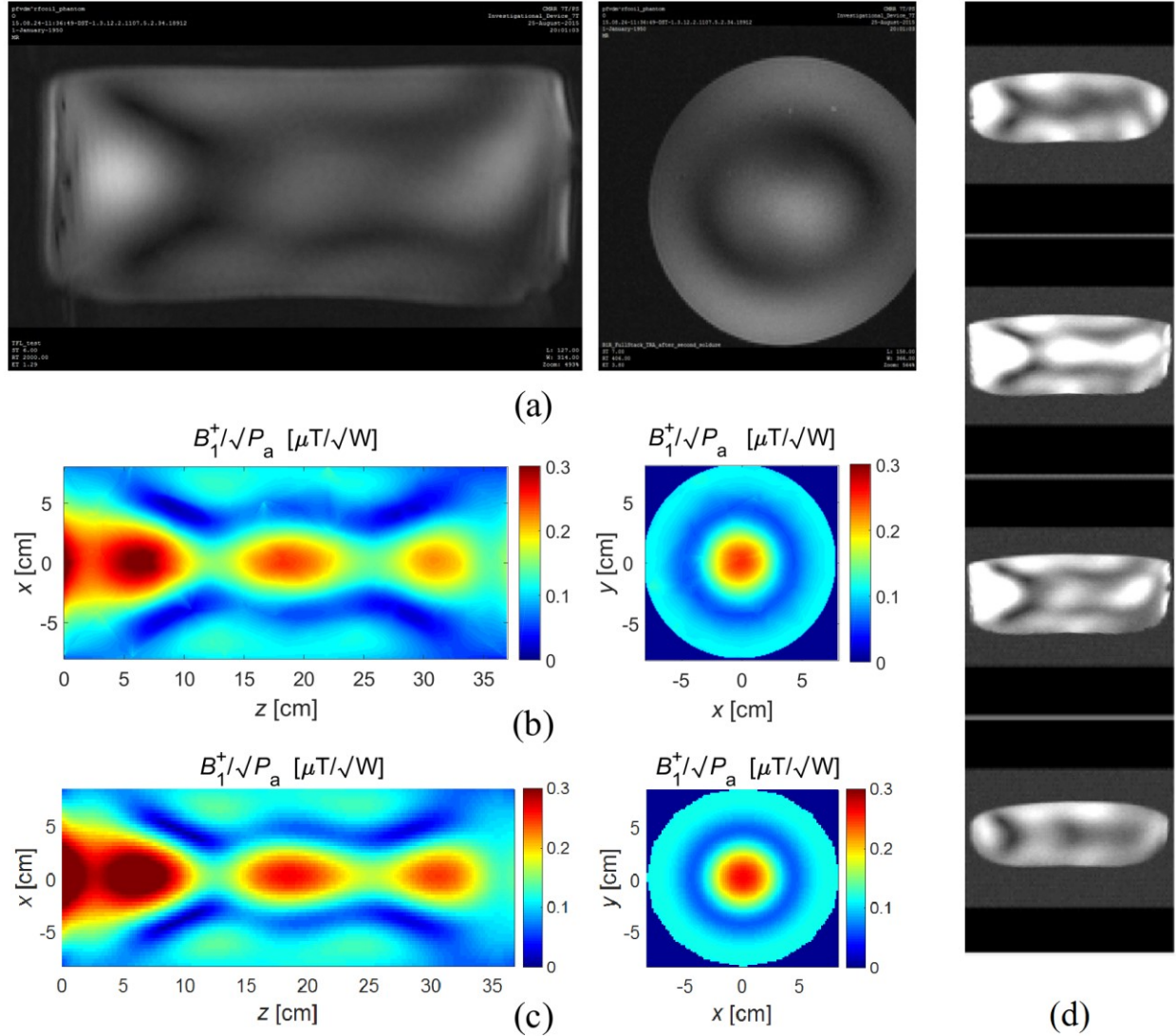
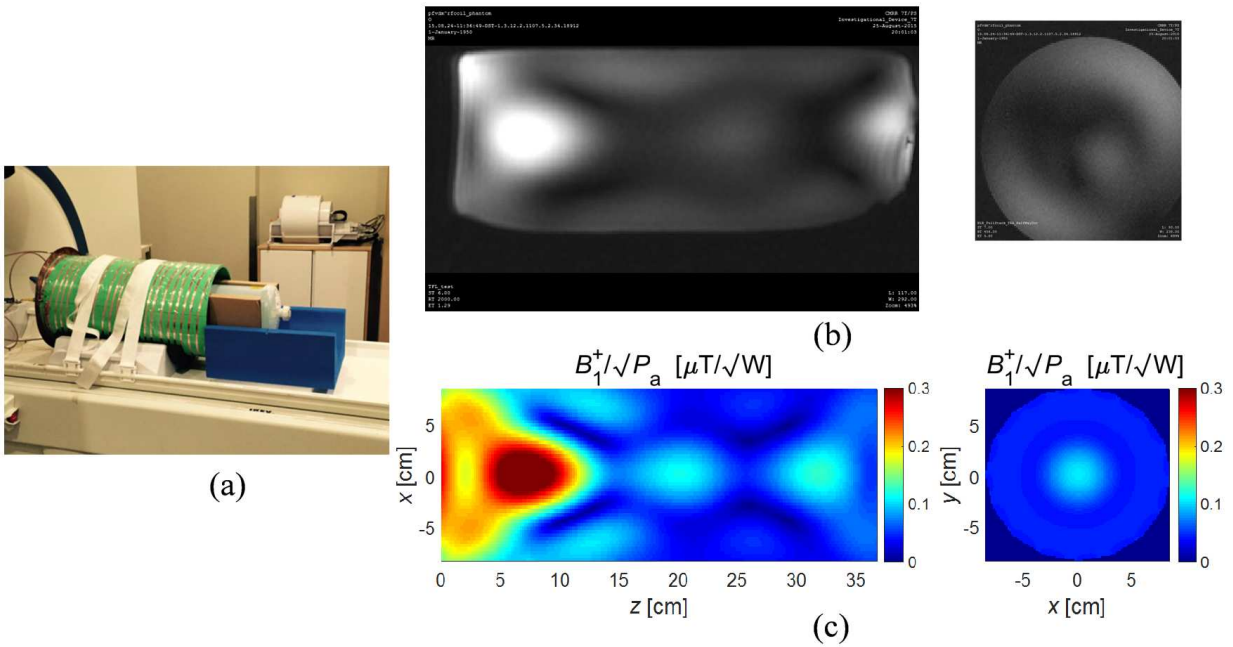


**Fig. 2.4.** Experimental and simulated central coronal and axial 2-D  $B_1$ -maps for a 4-channel helical antenna 7-T RF coil prototype, in Fig. 2.3(a), with a saline-water “bottle” phantom placed at the far end inside the coil (as in Fig. 2.2): (a) CMRR measurements (relative maps), (b) ANSYS-HFSS-computed  $B_1^+/\sqrt{P_a}$  (transmit efficiency), and (c) MoM-SIE-computed  $B_1^+/\sqrt{P_a}$  (transmit efficiency) in coronal and axial planes, respectively ( $P_a$  is the total accepted power); the computed maximum efficiency should be compared with the efficiencies in [39], [45]-[47]. (d) CMRR measured relative  $B_1$  field distributions in four different coronal slices with all four channels transmitting together.

**Table 2.1.**

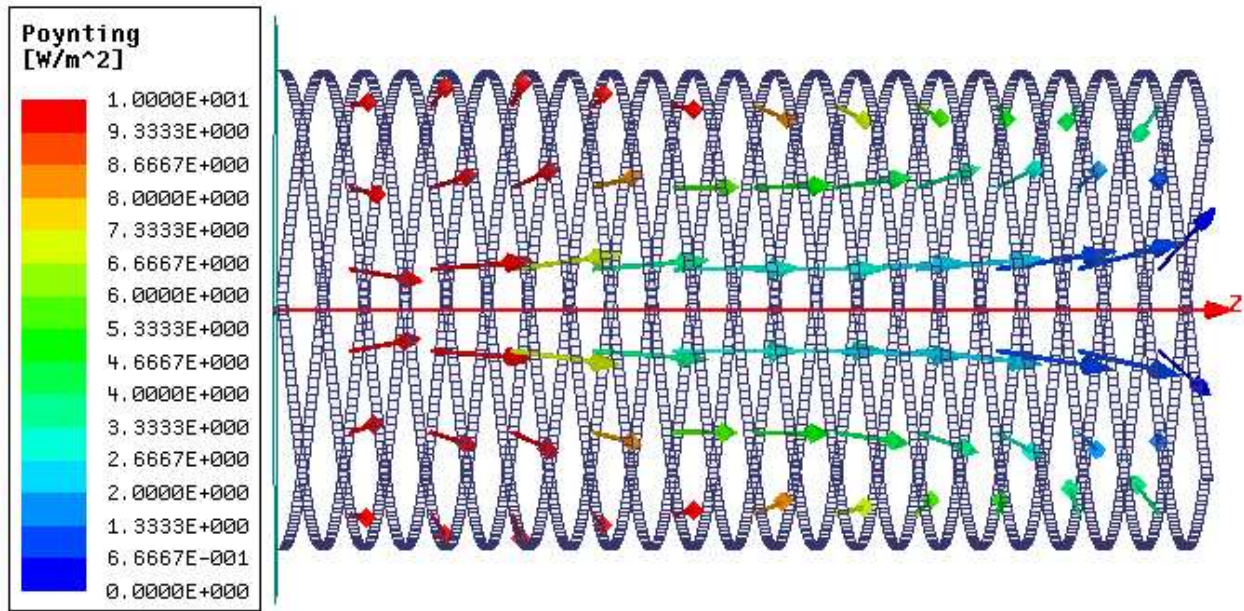
$D_{\text{helix}}$ (cm)	$L_{\text{helix}}$ (cm)	$P$ (cm)	$w_s$ (mm)	$D_{\text{plate}}$ (cm)	$D_p$ (cm)	$L_p$ (cm)	$\epsilon_r$	$\sigma$ (s/m)
32	60	10.7	6.35	38	17	37	81	0.6

As the first structure within the presented framework of multi-channel helical-antenna inner-volume RF coils, we consider a 7-T MRI system as shown in Fig. 2.1. Fig. 2.4 shows experimentally and numerically obtained data for a 4-channel helical-antenna 7-T RF coil prototype with a “bottle” phantom having parameters as shown in Table 2.1 (for  $L_{\text{bore}} = 336$  cm,  $D_{\text{bore}} = 90$  cm,  $f_0 = 300$  MHz, depicted in Fig. 2.3(a)). The phantom is placed at the far end inside the RF coil ( $d = 22$  cm), as in Fig. 2.2. The return loss, measured in free space, amounts to 13 dB, 10.61 dB, 28.72 dB, and 14.41 dB, respectively, at the four ports of the antenna prototype at  $f_0 = 300$  MHz w.r.t.  $50 \Omega$ . Shown in Fig. 2.4 are CMRR-measured and simulated central coronal and axial  $B_1$ -maps of the phantom, along with measured relative  $B_1$  field distributions in four different coronal slices with all four channels transmitting together. More specifically, Figs. 2.4(b) and 2.4(c) show the transmit efficiency evaluated using ANSYS-HFSS (FEM, volumetric, field modeling, code) and MoM-SIE (MoM, surface, current modeling, code), respectively, as  $B_1^+/\sqrt{P_a}$ , in coronal and axial planes, where  $P_a = P_{a1} + P_{a2} + P_{a3} + P_{a4}$  is the total accepted power for the coil, with  $P_{ai}$  standing for the individual power accepted by the  $i$ -th coil ( $i = 1, 2, 3, 4$ ). We observe qualitative agreements between the two sets of simulation results obtained using two completely different computational techniques and between simulation results and measurements. The measured power efficiency is acceptable, and the amount of power delivered to the imaged phantom is sufficiently high for all experiments and MRI processing. The computed maximum efficiency is comparable with those reported for other state-of-the-art coils at 7 T in [39], [45]-[47].



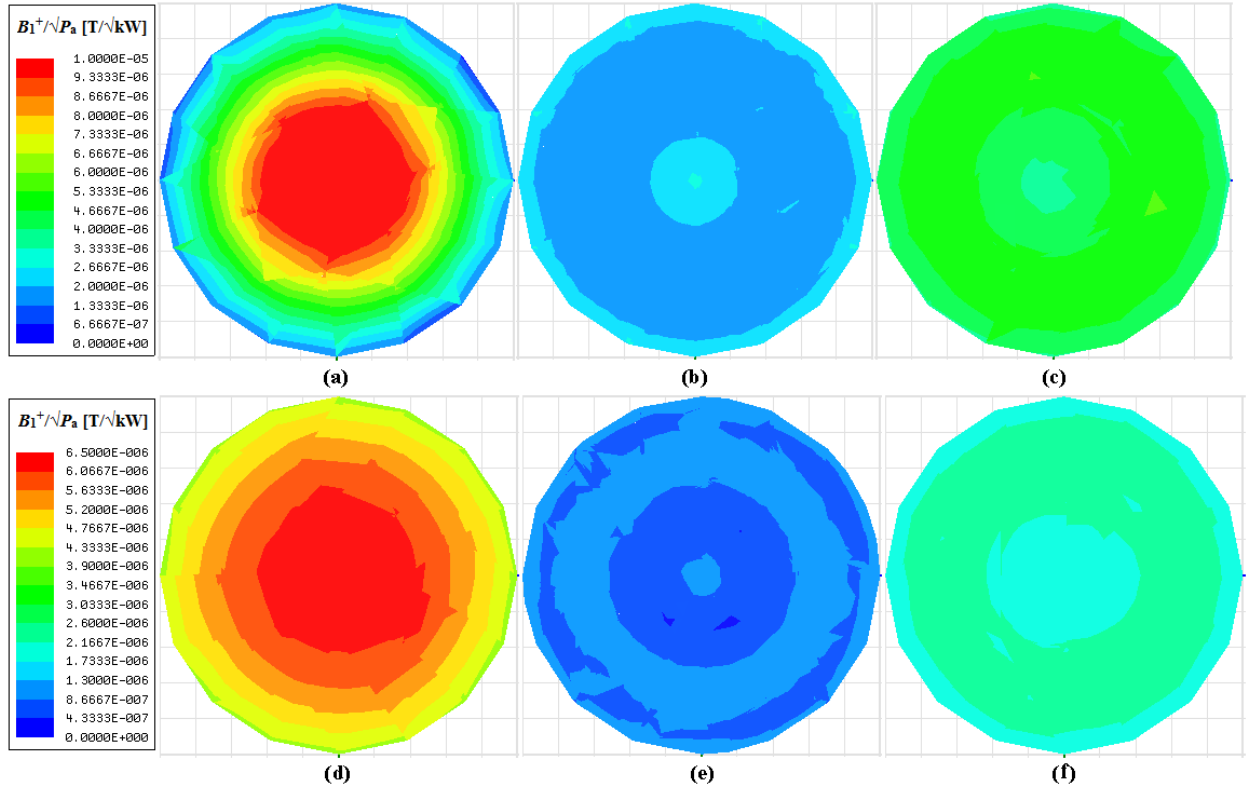
**Fig. 2.5.** (a) CMRR experiments at 7 T with the saline-water “bottle” phantom placed half inside and half outside the 4-channel helical-antenna RF coil prototype. (b) CMRR  $B_1$  measurements (relative maps). (c) MoM-SIE-computed  $B_1^+/\sqrt{P_a}$  (transmit efficiency) in coronal and axial planes of the phantom.

Fig. 2.5 shows the experimental and simulation results, namely, CMRR-measured relative  $B_1$  distribution and MoM-SIE-simulated  $B_1^+/\sqrt{P_a}$ -efficiency maps, for the phantom placed half inside and half outside the coil ( $d = 41$  cm). For this phantom placement, the power delivered to the half of the phantom inside the helix is noticeably higher than the power delivered to the half that is outside. On the other hand, these results demonstrate the far field component of the  $B_1$  field as it excites spins outside the coil volume. In addition, when the phantom is placed completely outside the coil, at its opening ( $d = 60$  cm), the power delivered to the phantom is still sufficient but considerably lower than when the phantom is completely inside the coil.



**Fig. 2.6.** Simulated Poynting vector in the coronal plane inside an unloaded 4-channel helical-antenna RF coil at 7 T.

Fig. 2.6 shows simulation results for the Poynting vector inside the 4-channel ( $M = 4$ ) 7-T helical-antenna RF coil described in the previous case but without any phantom inside the coil. The Poynting vector, for the most of the region inside the coil, is strongly aligned along the  $z$ -direction, indicating an overall forward traveling wave inside the antenna volume. This demonstrates utilization of the principles of a traveling-wave MRI coil, that is, it shows that the coil is a traveling-wave antenna.



**FIG. 2.7.** Simulated axial 2-D  $B_1^+/\sqrt{P_a}$  efficiency maps for the 4-channel helical-antenna coil at 7 T loaded with a cylindrical saline filled phantom, with (a)-(c) the entire phantom inside the RF coil and (d)-(f) half of the phantom inside and half outside the coil, for cuts at (a),(d) the proximal end, (b),(e) the central location, and (c),(f) the distant end, respectively. The maximum  $B_1^+/\sqrt{P_a}$  efficiency results should be compared with those in Fig. 4 of [45] for a standard traveling-wave setup.

We then compare the efficiency of the helical antenna design with some of the conventional and state-of-the-art designs at 7 T. We first compare our design with that of Brunner et al. [45], which may be considered a standard traveling-wave setup. Fig. 2.7 shows simulation results for  $B_1^+/\sqrt{P_a}$  efficiency maps of a 4-channel helical-antenna coil in axial cuts at three positions, namely, at the proximal end, central location, and distant end. The coil is the same as in the previous case shown in Fig. 2.5, and it is loaded by a cylindrical saline filled phantom with  $L_p = 34$  cm,  $D_p = 10$  cm,  $\epsilon_r = 81$ , and  $\sigma = 0.84$  S/m in Fig. 2.1(b). Figs. 2.7(a)-(c) show  $B_1^+/\sqrt{P_a}$  efficiency maps for the phantom placed at a distance  $d = 16.1$  cm from the backplate, with the entire phantom inside the RF coil, while Figs. 2.7(d)-(f) show efficiency maps for the phantom placed at a distance  $d = 43.1$  cm from the backplate, with half of the phantom

inside and half outside the coil. The maximum  $B_1^+/\sqrt{P_a}$  efficiencies in both these cases are similar and comparable to the efficiency shown in Fig. 4 of [45].

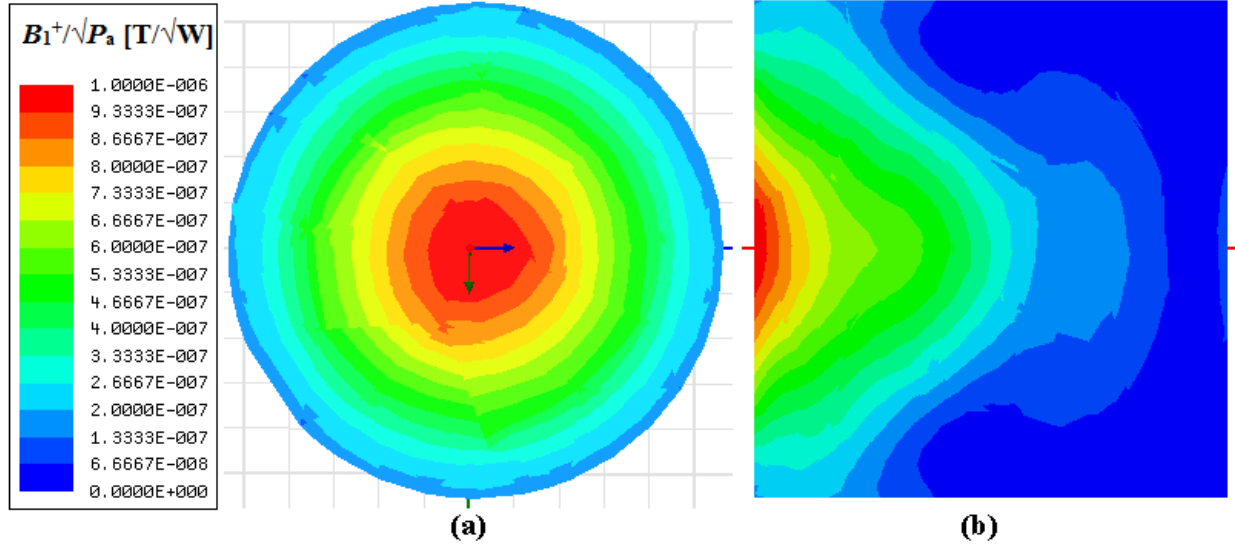


**Fig. 2.8.** Simulated (a) proximal-end axial and (b) sagittal 2-D  $B_1^+/\sqrt{P_a}$  efficiency maps of a cylindrical phantom as in [65] placed inside a 4-channel 7-T helical-antenna coil. The maximum  $B_1^+/\sqrt{P_a}$  efficiency should be compared with that in Fig. 12 of [65] for the microstrip transmission line (MTL) coil.

**Table 2.2.**

$D_{\text{helix}}$ (cm)	$L_{\text{helix}}$ (cm)	$P$ (cm)	$w_s$ (mm)	$D_{\text{plate}}$ (cm)	$D_P$ (cm)	$L_P$ (cm)	$\epsilon_r$	$\sigma$ (s/m)
27	30	10.67	6.35	40	22	21	58.1	0.539

Next, shown in Fig. 2.8 are simulation results for proximal-end axial and sagittal  $B_1^+/\sqrt{P_a}$  efficiency maps of a 4-channel 7-T helical-antenna design with parameters as given in Table 2.2. for  $L_{\text{bore}} = 336$  cm,  $D_{\text{bore}} = 90$  cm,  $f_0 = 300$  MHz aimed for comparison with the results of the microstrip transmission line (MTL) coil shown in Sohn et al. [65] (their Fig. 12). The phantom inside the helix coil is modeled to mimic the cylindrical phantom from [65] as accurately as possible with  $L_P = 21$  cm,  $D_P = 22$  cm,  $\epsilon_r = 58.1$ , and  $\sigma = 0.539$  S/m in Fig. 1(b), and is positioned at a distance  $d = 9.1$  cm from the backplate, i.e., at the far end of the helix (the far end of the phantom is at the far end of the coil). Note that this case also represents a potential head imaging situation. We see that the maximum  $B_1^+/\sqrt{P_a}$  efficiency

of the helical-antenna coil in Fig. 2.8, being  $1.15 \mu\text{T}/\sqrt{W}$ , is comparable to that of the MTL coil shown in Fig. 12 of [65] which is  $\sim 0.6 \mu\text{T}/\sqrt{W}$ .

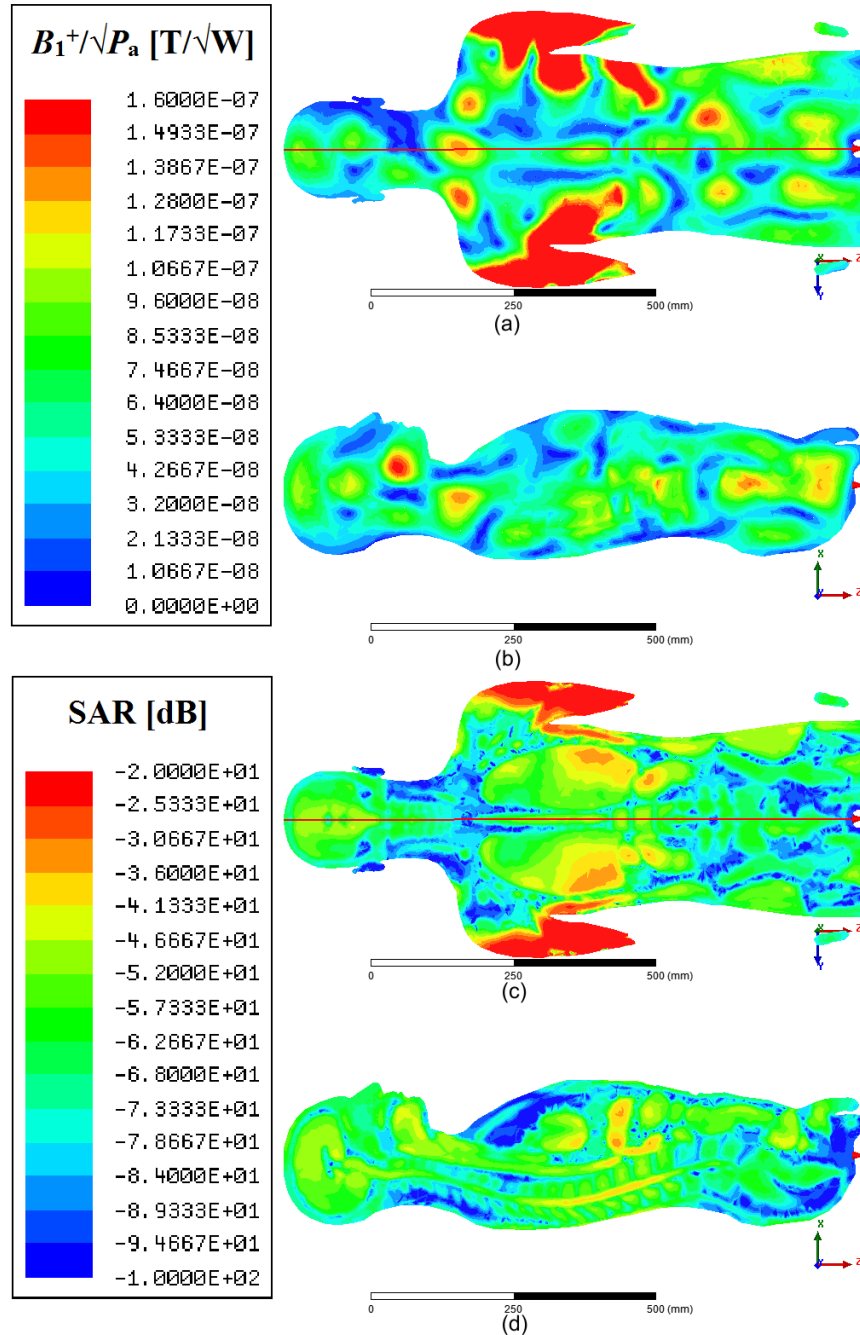


**Fig. 2.9.** Illustration of the potential applicability of the helical-antenna coil as a volume body UHF coil: simulation results for (a) coronal  $B_1^+/\sqrt{P_a}$  efficiency map, (b) sagittal  $B_1^+/\sqrt{P_a}$  efficiency map, (c) coronal SAR map, and (d) sagittal SAR map of an inhomogeneous realistic human body model placed inside a wider variant of the 4-channel 7-T helix coil. The  $B_1^+/\sqrt{P_a}$  efficiency and SAR results were compared with those reported in Figs. 9 and 11, respectively, in [47] for a similar human body model.

In order to demonstrate the applicability of the helical-antenna coil as a volume body UHF coil, Figs. 2.9(a) and (b) show simulation results for  $B_1^+/\sqrt{P_a}$  efficiency maps of a wider variant of the 4-channel 7-T helical-antenna coil design, namely, of a 54-cm wide helix (Fig. 1:  $L_{\text{bore}} = 336$  cm,  $D_{\text{bore}} = 90$  cm,  $L_{\text{helix}} = 60$  cm,  $D_{\text{helix}} = 54$  cm,  $P = 10.67$  cm,  $w_s = 6.35$  mm,  $D_{\text{plate}} = 60$  cm,  $f_0 = 300$  MHz), loaded with a human body model. The model used for the simulation is a detailed inhomogeneous layered model of a human body made of 30 different lossy dielectrics (plus air) for various tissues, cavities, fluids, etc. The model is that of a male human and is 183 cm (6 feet) at its longest, i.e., from the head top to feet bottom, and 52 cm at its widest, i.e., from one arm to the other. The body model is placed inside the coil at a distance  $d = 6$  cm away from the backplate. The  $B_1^+/\sqrt{P_a}$  efficiency results are similar and comparable in value and distribution to those calculated from the results and input power of Zhang et al. [47] in their Fig. 7, where a similar human body model was used and it was shown that the  $B_1^+$  field is sufficient for successful imaging. Moreover, it can be seen from Figs. 2.9(a) and (b) that the field efficiency in the bulk of the torso is higher in the case of the helical antenna, i.e.,  $\sim 0.09 \mu\text{T}/\sqrt{\text{W}}$ , compared to  $\sim 0.075 \mu\text{T}/\sqrt{\text{W}}$  in [47] (Fig. 9). With reference to the SAR maps shown in Figs. 2.9(c) and (d), we can see that the SAR values for the helical-antenna coil are for the most part lower than or equal to those of Zhang et al. [47] in their Fig. 11.

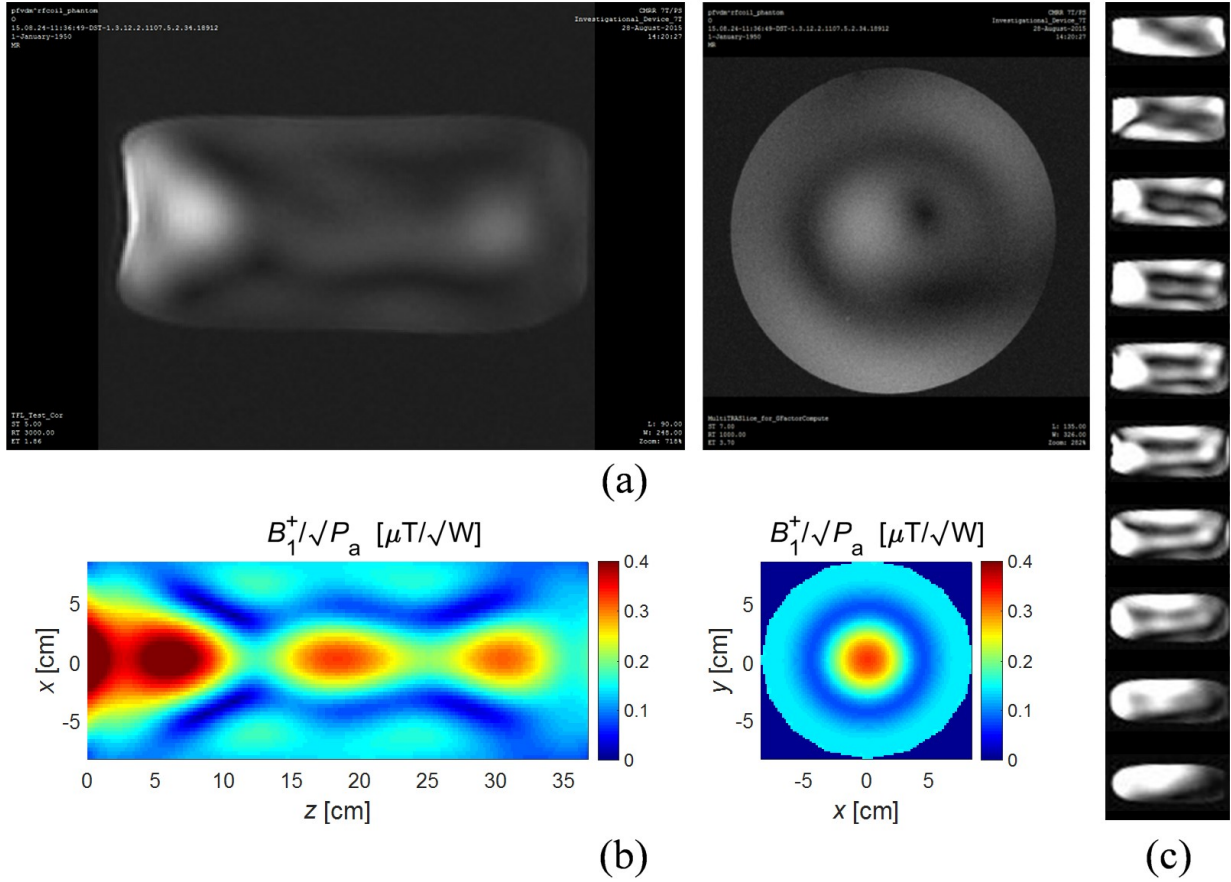


**Fig. 2.10.** (a) CMRR-measured relative  $B_1$  maps and (b) MoM-SIE-simulated  $B_1^+/\sqrt{P_a}$  efficiency maps in central coronal and axial planes for an octafilar (8-channel) helical-antenna coil prototype at 7 T, in Fig. 2.3(b), with the saline-water “bottle” phantom placed at the far end inside the coil (Fig. 2.2). (c) Experimental relative  $B_1$  field distributions in ten different coronal slices with all eight channels transmitting together.

**Table 2.3.**

$D_{\text{helix}}$ (cm)	$L_{\text{helix}}$ (cm)	$P$ (cm)	$w_s$ (mm)	$D_{\text{plate}}$ (cm)	$D_P$ (cm)	$L_P$ (cm)	$d$ (cm)	$\epsilon_r$	$\sigma$ (s/m)
32	65	10.7	6.35	38	17	37	22	81	0.6

Fig. 2.10 shows CMRR-measured relative  $B_1$  distribution and MoM-SIE-simulated  $B_1^+/\sqrt{P_a}$ -efficiency maps in the central coronal and axial slices for an octafilar, 8-channel ( $M = 8$ ), helical-antenna coil prototype at 7 T with parameters as given in Table 2.3 for  $L_{\text{bore}} = 336$  cm,  $D_{\text{bore}} = 90$  cm,  $f_0 = 300$  MHz, depicted in Fig. 3(b), as well as the measured  $B_1$  field distributions in ten different coronal slices with all eight channels transmitting together. Similar observations, as for Fig. 2.4, are made, from Fig.

2.10, for the 8-channel helical-antenna 7-T coil. The computed transmit efficiency of the octafilar helix is ~25% higher than that of the quadrifilar one.

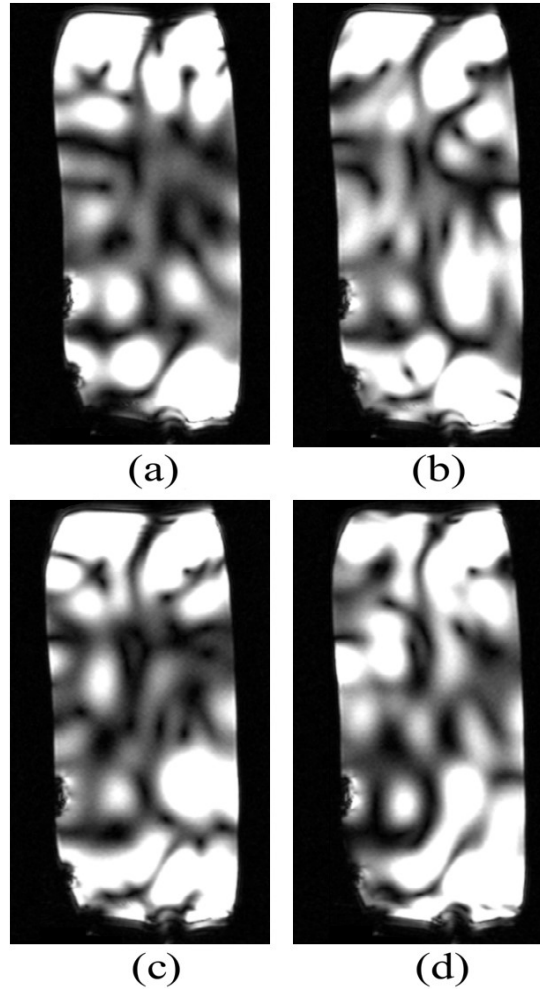


**Fig. 2.11.** CMRR-measured relative  $B_1$ -maps for a 4-channel helical-antenna RF coil prototype at 10.5 T, in Fig. 2.3(c), with the saline-water “bottle” phantom placed at the far end inside the coil (as in Fig. 2.2): (a)–(d) magnitude image (GRE, sagittal slice) from each of the four receive channels (RF transmission on all channels without specific transmit phase adjustment).

**Table 2.4.**

$D_{\text{helix}}$ (cm)	$L_{\text{helix}}$ (cm)	$P$ (cm)	$w_s$ (mm)	$D_{\text{plate}}$ (cm)	$D_p$ (cm)	$L_p$ (cm)	$d$ (cm)	$\epsilon_r$	$\sigma$ (s/m)
21	60	16	6.35	38	17	37	22	81	0.6

As the last structure, we consider a 4-channel helical-antenna RF coil prototype at 10.5 T with the saline-water “bottle” phantom placed at the far end inside the coil with parameters as given in Table 2.4

for  $L_{\text{bore}} = 410$  cm,  $D_{\text{bore}} = 90$  cm,  $f_0 = 443$  MHz, shown in Fig. 2.3(c). The free-space return loss w.r.t.  $50 \Omega$  is measured, at  $f_0 = 443$  MHz, to be 10.63 dB, 11.83 dB, 14.48 dB, and 20.4 dB, respectively, at the four ports of the antenna prototype. Shown in Fig. 2.11 are the results from CMRR experiments for the relative  $B_1$  field distribution in the sagittal cross section of the phantom – magnitude images from each of the four receive channels, with RF transmission on all channels. Note that 10.5-T experiments are done without proper phasing of the four excitation ports of the coil, with which circular polarization would be further enhanced. Overall, experimental results at 10.5 T demonstrate the scalability and versatility of the UHF-MR helix coil design as was demonstrated in 3 T and 7 T.

## 2.4 Conclusion

The main outcome of the multi-channel helical-antenna inner-volume coil development presented in the paper [60] is to provide improved RF performance for UHF MRI while preserving the ease of use of a volume coverage coil. The inner volume of a helical-antenna structure is utilized to image a sample (conventional helix coils are utilized as a TW CP source with the target sample outside of the coil). This design benefits from the congruence of two regimes: a far-field regime that concerns the current path over the wires of the coil and a near-field regime that is involved in local interactions between the sample and the coil wires. Furthermore, multiple channels are utilized (4 and 8 in the prototype configurations) to enable all multi-transmit channel RF technology.

The presented phantom data obtained at 7 T show good qualitative consistency between numerical simulations and experimental results with 4- and 8-channel helix coils. The numerical results for the maximum  $B_1^+/\sqrt{P_a}$  efficiency of helical-antenna RF coils are comparable to or higher than those of some of the conventional and state-of-the-art coil designs at 7 T. The 10.5-T machine at CMRR used for this work is the first (and only, as of today) operational human-size MRI scanner reaching 10.5 T. The experimental results show the scalability of the helix coil design from 3T and 7 T to 10.5 T.

### 3 SLOTTED-WAVEGUIDE ARRAY COIL

#### 3.1 Introduction

The slotted-waveguide array (SWGA) coil for 7 T MRI is a novel concept first presented by M. M. Ilić and B. M. Notaroš in [66]. This approach uses a set of slotted i.e. leaky waveguides designed to excite strong  $B_1^+$  field inside the imaged sample place along their length with linear polarization. When phased as an array, the set of slotted-waveguides generate a very strong  $B_1^+$  field. The simulation results for the slotted-waveguide array were compared with a transverse electromagnetic (TEM) coil, one of the best state-of-the-art MRI coils, and the SWGA were shown to outperform the TEM coil.

#### 3.2 Materials and Methods

A slotted waveguide is made by milling slots on the conducting walls of a rectangular waveguide [67]. The slots are milled in order to achieve the desired leaky waveguides. The exact method is elaborated in [66]. Based on [66] we fabricated a three element SWGA. In order to reduce the size of the SWGA elements and the entire assembly, the slotted-waveguides were designed assuming it to be filled with distilled water ( $\epsilon_r = 81$ ). Based on the dimensions from [66], aluminum slotted-waveguides were fabricated. SMA connectors with copper probes connected to the end were inserted into the waveguide in order to excite the desired TE<sub>10</sub> mode.

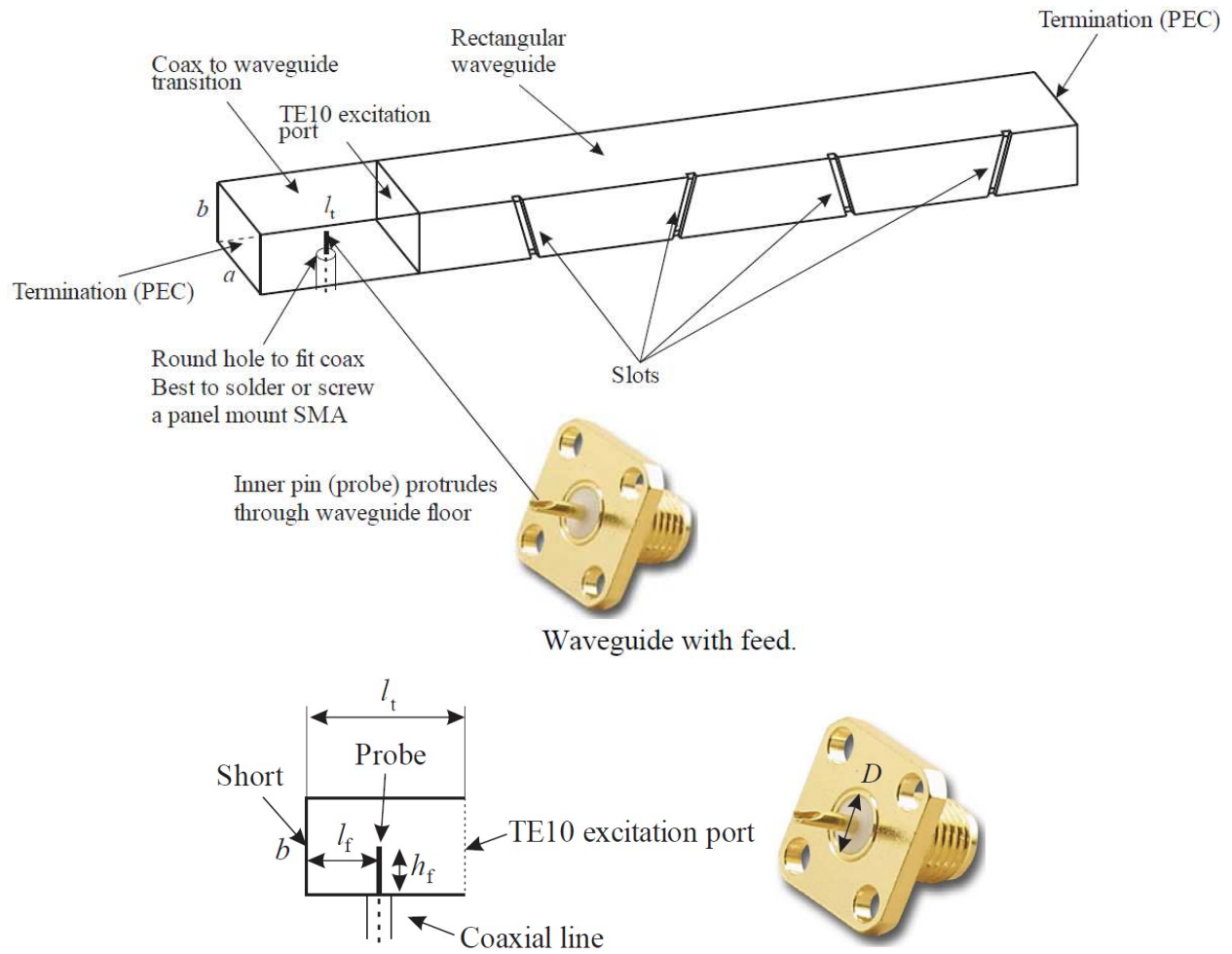


**Fig. 3.1.** Figures and photograph of the slotted-waveguide and the placement of the SMA connector as a probe.

The waveguide slots were sealed with ABS plastic plugs and epoxy. The waveguides were then filled with distilled water.. In order to minimize the return loss on the power and in turn maximize  $B_1^+$ , matching circuits were designed by measuring the range of impedance mismatch on a network analyzer. The matching circuits were tuned to achieve  $|S_{11}|$  less than -35 dB.

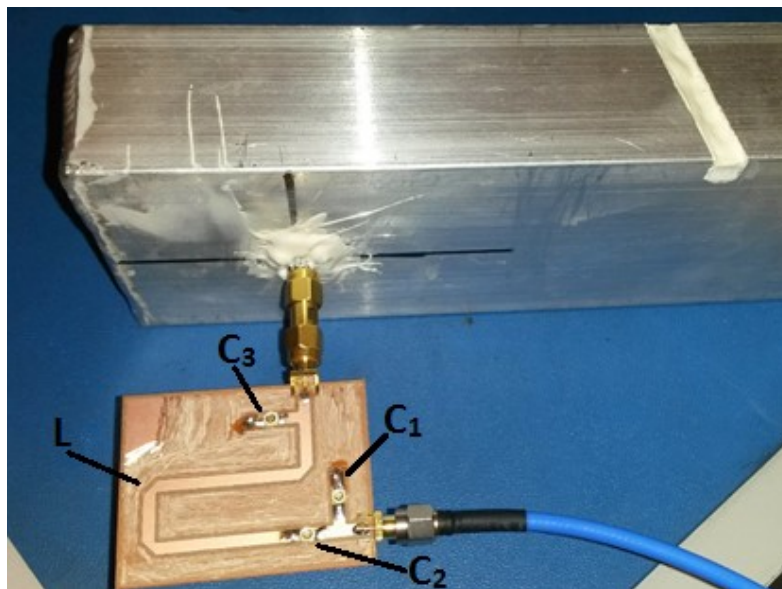
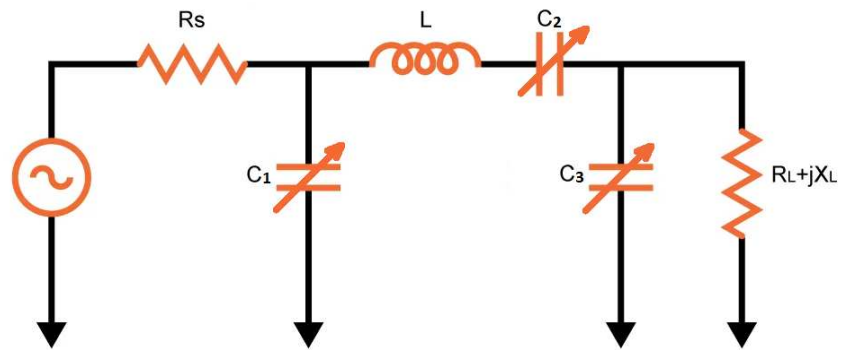


**Fig. 3.2.** Schematic diagram along with the fabricated impedance matching network connected to a slotted-waveguide.



**Fig. 3.3.** Three element SWGA assembly.

The three element SWGA was simulated in ANSYS HFSS with the same saline filled phantom as used in the 7 T helix chapter 3. In order to verify the results experimental measurements were carried out for the SWGA shown in Fig. 3.3 in the 7 T scanner at the Center for Magnetic Resonance Research (CMRR), University of Minnesota.

### 3.3 Results and Discussion

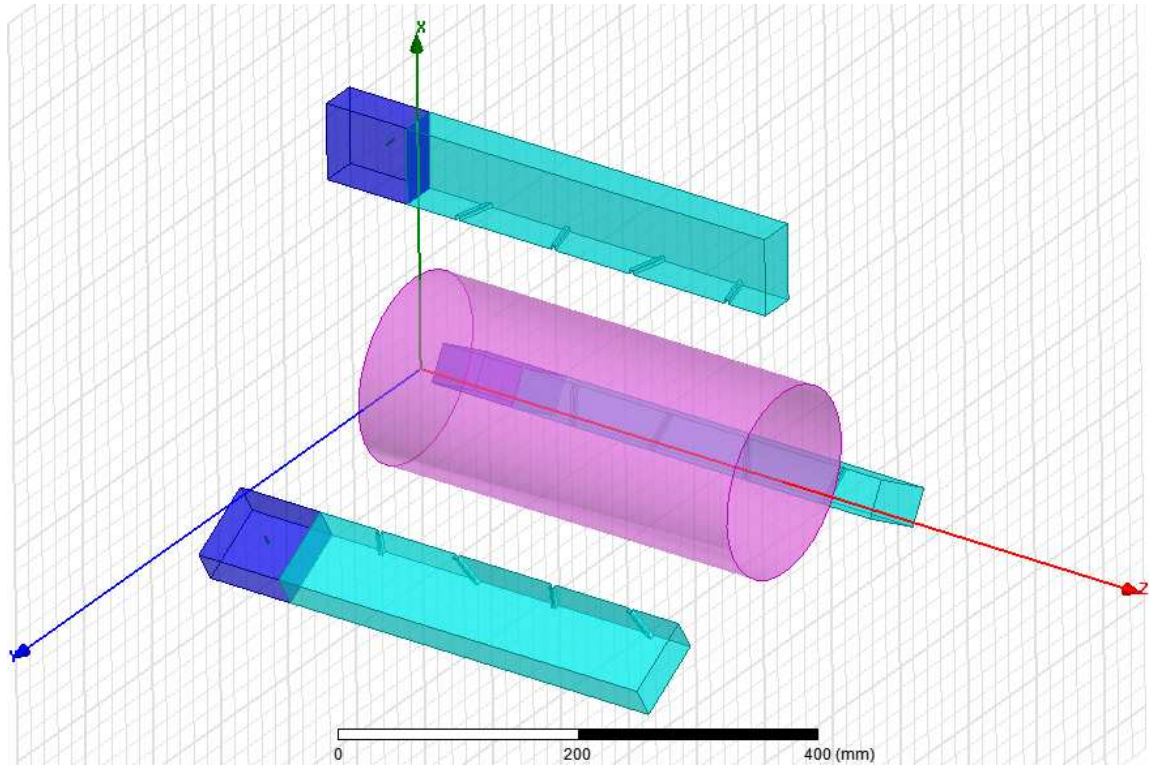


**Fig. 3.4.** HFSS model of the 3 element slotted waveguide array around the saline filled cylindrical phantom.

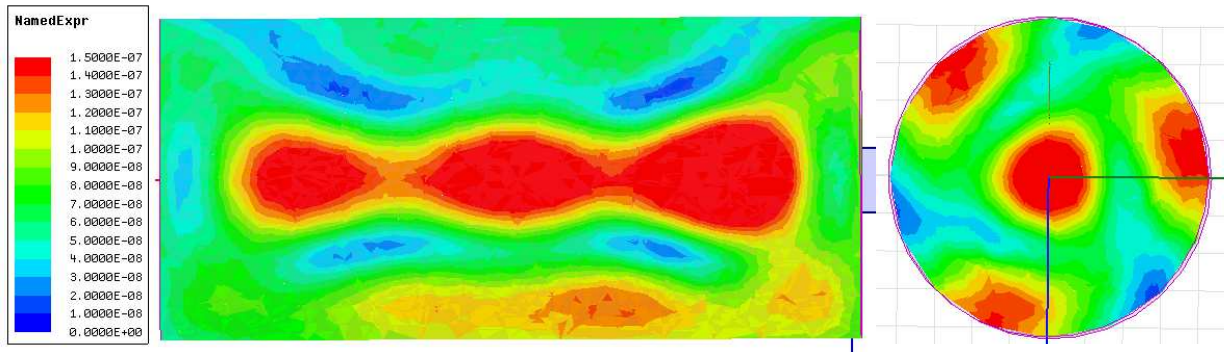


**Fig. 3.5.** Simulated transmit efficiency  $B_1^+/\sqrt{P_{\text{accepted}}}$  [T/ $\sqrt{W}$ ] inside the phantom in the Coronal and Axial plane, without dielectric lenses.

The simulated transmit efficiency of the SWGA is acceptable for a successful scan i.e. in the range of values seen in Section 2. However, we were unable to reproduce the theoretical results during the experimental measurements. Presence of very strong Eddy currents caused extreme distortion and we were unable to receive any substantial signal.

### 3.4 Conclusion

Even though the SWGA as shown in [66] is a very sound concept for RF coils; several practical obstacles made it difficult to test it in the 7-T scanner. The waveguides, having been made of one single piece of solid aluminum provides large and continuous surface for Eddy currents to appear. These Eddy currents distort the static  $\mathbf{B}_0$  field causing heavy distortions. Additionally, the dielectric i.e. distilled water contributes a strong MR signature close to the probe and could also be masking the signal from the saline phantom.

## 4 IMPROVING RF FIELD EFFICIENCY AND HOMOGENEITY USING DIELECTRIC LOADING

### 4.1 Dielectric Loading in Traveling Wave MRI

The next-generation magnetic resonance imaging (MRI) systems at ultra-high static magnetic fields (magnetic flux densities),  $B_0 > 3$  T, and ultra-high Larmor frequencies,  $f_0 > 127.8$  MHz, utilize RF excitation magnetic fields,  $\mathbf{B}_1$ , in the form of traveling waves (TWs) in the MRI bore [68]. Hence, the images of subjects are generated and received by far-field coils, namely, by excitation probes that essentially operate as antennas, in place of the traditional quasi-static, near-field RF coils used in 3-T clinical MRI scanners (e.g., birdcage coils). When compared to traditional, quasi-static, MRI systems, TW MRI systems can provide more homogeneous  $\mathbf{B}_1$  field distribution, better signal-to-noise ratio, larger field of view, more comfort for patients, etc. Moreover, it is possible to potentially benefit from the advantages of TW concepts are at relatively lower (but still considered high) field strengths (e.g.,  $B_0 = 3$  T;  $f_0 = 127.8$  MHz), in order to address challenges and enable substantial improvements of current clinical MRI scanners at 3 T. The generation and control of TW  $\mathbf{B}_1$  RF fields inside a MRI bore and a phantom or a subject under MRI imaging are very challenging tasks. There has been limited work done on TW excitation using loops, dipole antennas, and microstrip patch antennas. as antenna probes. Such excitations of TW are highly localized, which results in rapid power dissipation in the body and thus in high local specific absorption rate (SAR) levels in regions of the body and rapid attenuation with distance away from the antenna. However, one approach to improve the TW  $\mathbf{B}_1$  RF fields inside a MRI bore, loaded with a human (or animal) body or body part or phantom, is to incorporate various dielectric and other material loadings into the bore, in order to reduce the cutoff frequencies of the bore viewed as a metallic circular waveguide, enable traveling waves along the bore, and control the field in the bore and the phantom [45], [69].

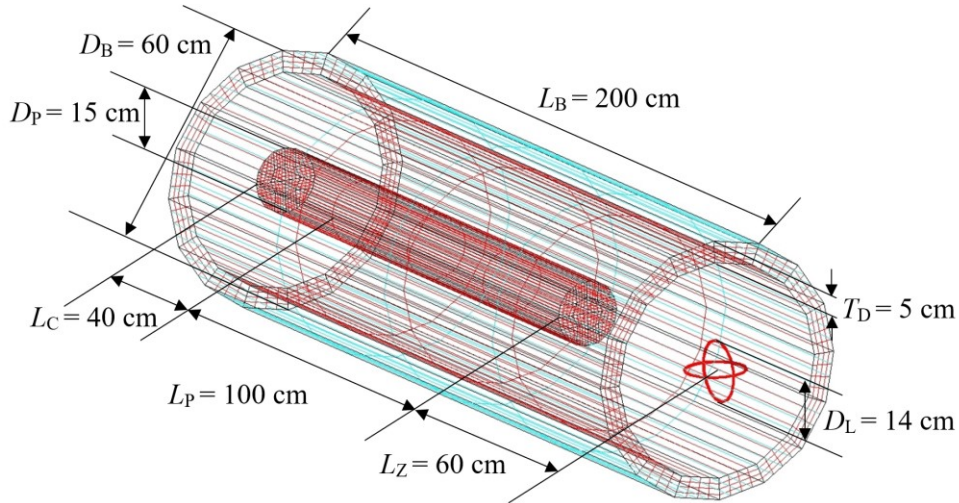


**Fig. 4.1.** 3-T system with saline phantom and a dielectric bore liner excited by orthogonal loops.

The 3-T system shown in the WIPL-D simulation in Fig. 4.1 has a bore that is 60 cm wide and 200 cm long. The phantom used is a saline ( $\epsilon_r = 81$ ,  $\sigma = 0.6$  S/m) cylindrical phantom of length 100 cm and 15 cm diameter with a 40 cm saline buffer on the end farther away from the orthogonal set of RF loop coils. It can be seen from Fig. 4.2 and Fig. 4.3 that adding a 5 cm thick dielectric ( $\epsilon_r = 132$ ,  $\sigma = 0.03$  S/m) linear along the bore walls significantly improves the field intensity and homogeneity along the phantom.

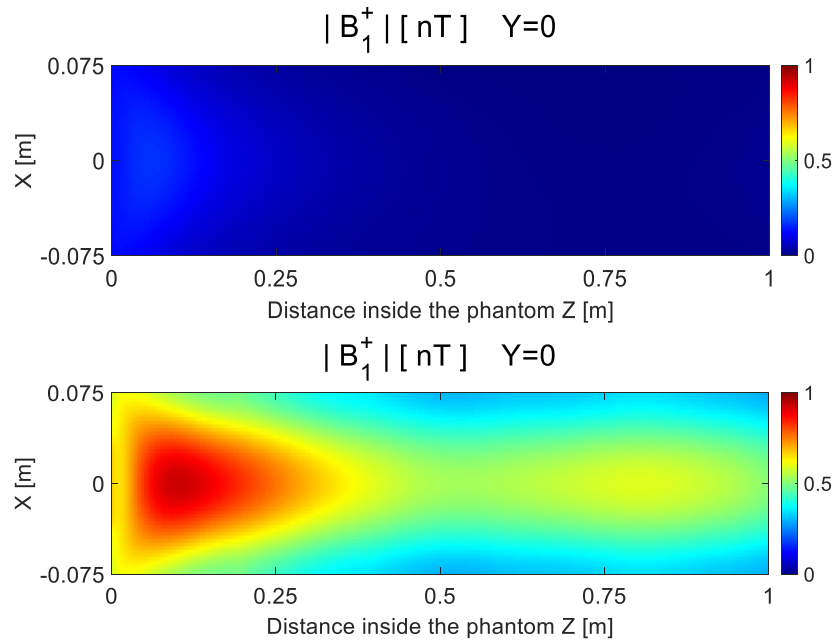


**Fig. 4.2.**  $B_1^+$  in  $xz$ -plane (sagittal/coronal) inside the phantom without dielectric liner(top) and with dielectric liner(bottom).

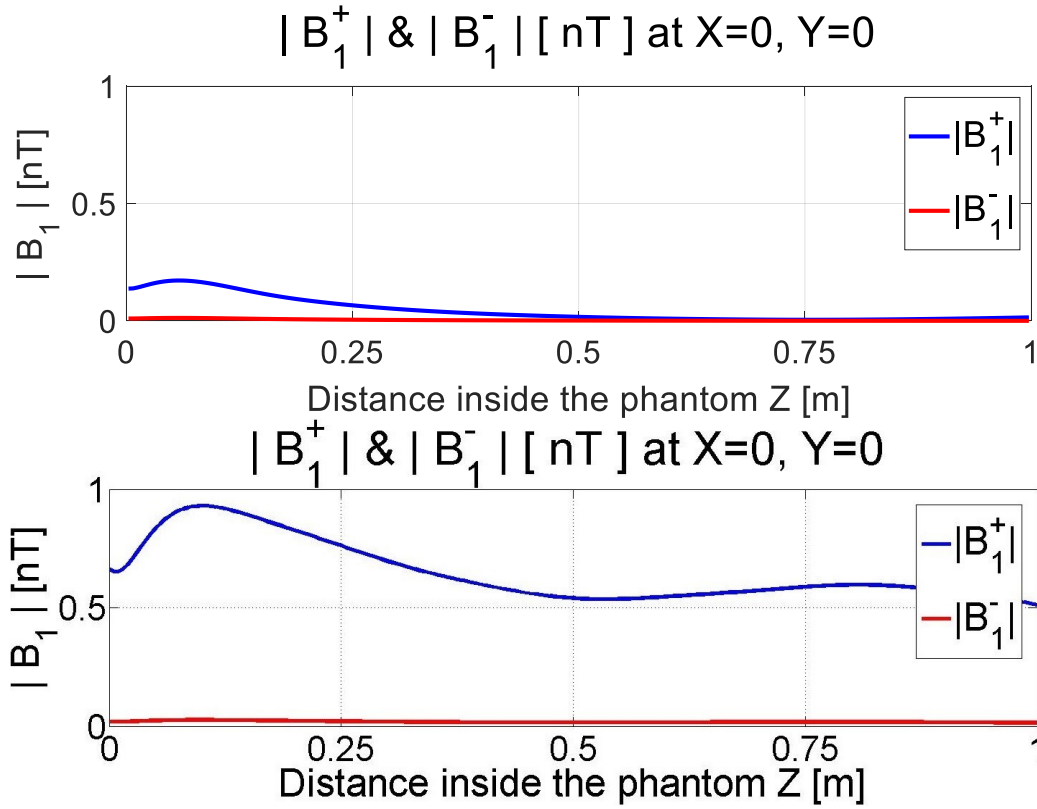


**Fig. 4.3.**  $B_1^+$  along z-axis inside the phantom without dielectric liner(top) and with dielectric liner(bottom)

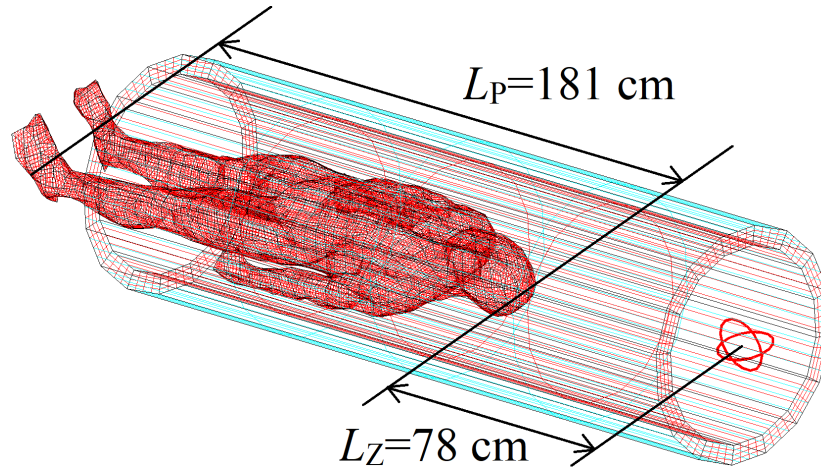


**Fig. 4.4.** 3-T system with saline human body phantom and a dielectric bore liner excited by orthogonal loops

Replacing the cylindrical phantom with saline human body phantom also produces similar results.

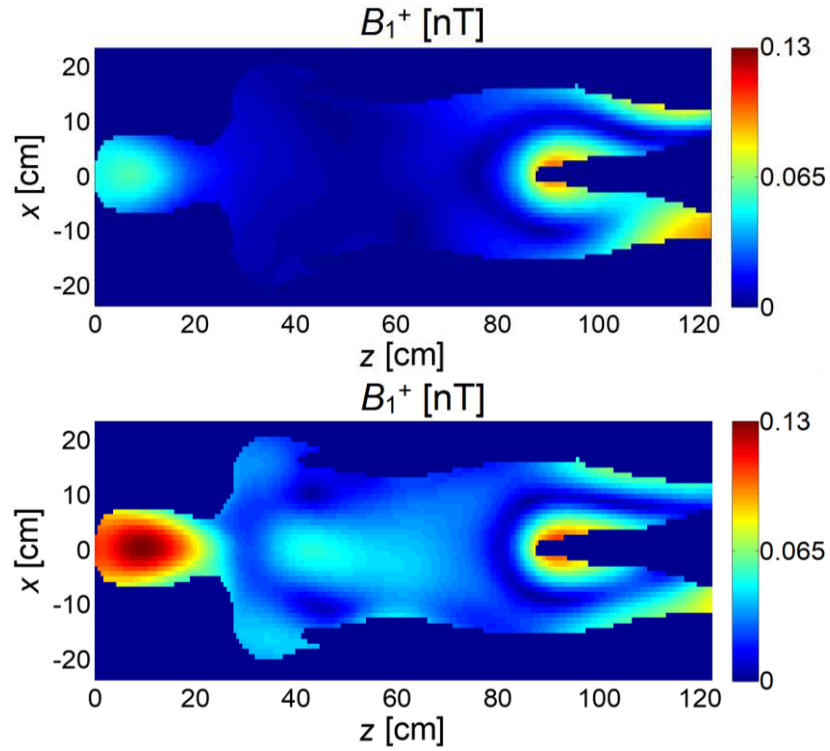


**Fig. 4.5.**  $B_1^+$  in  $xz$ -plane (coronal) inside the saline human body phantom without dielectric liner(top) and with dielectric liner(bottom).

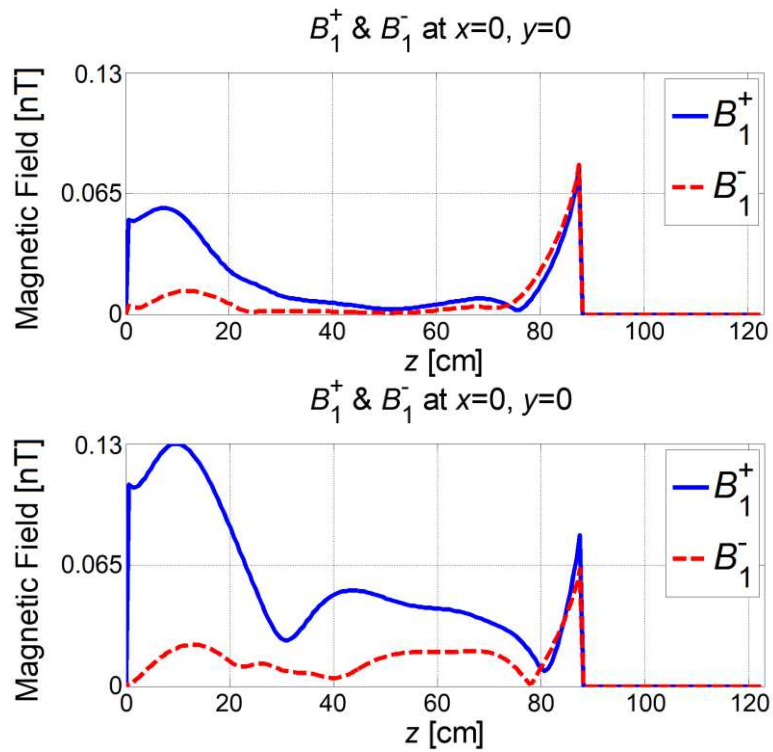


**Fig. 4.6.**  $B_1^+$  along  $z$ -axis inside the saline human body phantom without dielectric liner(top) and with dielectric liner(bottom).

## 4.2 Using Dielectric Loading as Buffer

In [31] we present how sudden and sharp changes in the dielectric along path of the traveling wave inside a phantom can give rise to wave reflections resulting in a highly inhomogeneous field pattern which is not desirable. This can be mitigated by using dielectric buffers.

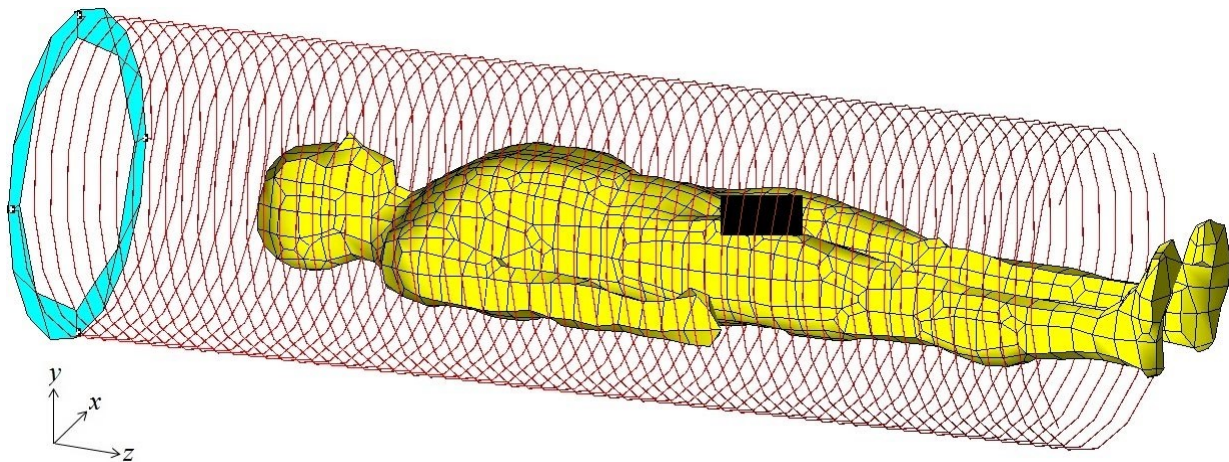


**Fig. 4.7.** MoM-SIE simulation model of a homogeneous human body phantom (parameters given in the text) inside a 60-cm 3-T MRI bore in Fig. 1.2 (the bore is not shown for clarity) with the same quadrifilar helical RF body coil as in Fig. 1.6 but terminated with a hollow back-plate (ring).

As in chapter 1, we simulate a human body shaped phantom inside a 60-cm 3-T MRI bore in Fig. 1.2 with the same quadrifilar helical RF body coil as in the example as shown in Fig 1.7. For practical reasons, the quadrifilar helical antenna (the four helices) is terminated with a hollow back-plate (ring) with  $D_{\text{plate1}} = 60$  cm and  $D_{\text{plate2}} = 50$  cm, placed outside the bore, 1.5 cm away from the bore opening. A homogeneous human-body MoM-SIE model of height/length  $L_{\text{body}} = 184$  cm and maximum width  $w_{\text{body}} = 52$  cm, filled with a lossy dielectric of averaged tissue parameters amounting to  $\epsilon_r = 31$  and  $\sigma = 0.31$  S/m [72], is placed 35 cm inside the bore (measured from the bore opening to the top of the head), as shown in Fig. 4.7 (the bore is not shown for the clarity of the figure). These tissue parameters are calculated in [72] by finding a volumetric average of two lossy-dielectric patient models. The accepted powers at the excitation ports 1–4 (Fig. 1.2) amount to  $P_{a1} = 35.99$  W,  $P_{a2} = 20.83$  W,  $P_{a3} = 34.89$  W, and  $P_{a4} = 30.48$  W, respectively.

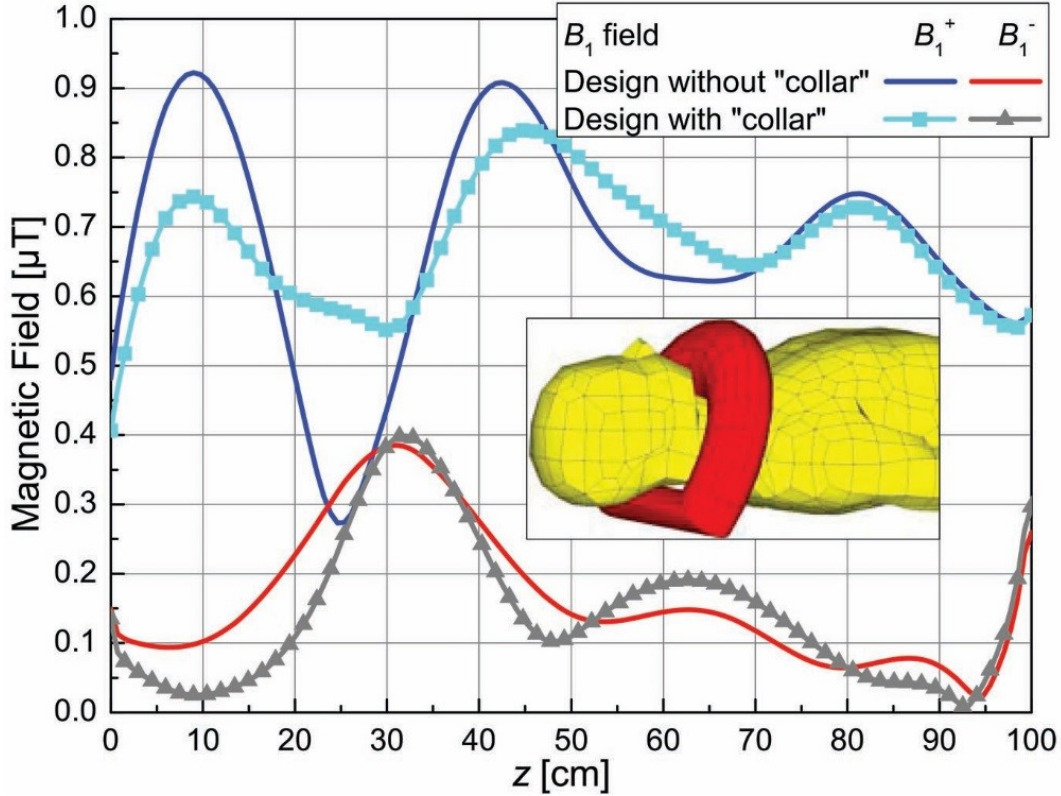


**Fig. 4.8.** Computed 1-D distribution of  $B_1^+$  and  $B_1^-$  efficiency inside the human body model in Fig. 1.8 along its central axis ( $z$ -axis) (from the top of the head to the end of the torso), without and with the dielectric “collar” (of the same dielectric properties as the phantom) around the neck, to mitigate the degradation in the field uniformity and circular polarization around the neck region. Detail of the human body model with the “collar” is shown in the figure inset.

Shown in Fig. 4.8 is the 1-D distribution of the  $B_1^+$  and  $B_1^-$  transverse fields along the central axis ( $z$ -axis) of the human body model from the top of the head to the end of the torso, where we observe a very small  $B_1^-$  compared to  $B_1^+$  and reasonable spatial uniformity of the  $B_1^+$  field along the  $z$ -axis everywhere, from the top of the head to the end of the torso, except in the neck area ( $z \approx 20\text{--}30$  cm). In order to mitigate the degradation in the field uniformity and circular polarization around the neck region, we add a “collar” (of the same dielectric properties as the human body phantom) around the neck, as shown in the inset of Fig. 4.8, and include in Fig. 4.8  $B_1^+$  and  $B_1^-$  1-D results for the phantom model with the “collar” as well. Note that a similar idea of using a “collar” to improve the field distribution has been suggested in [73]. As can also be seen from Fig. 4.8, the “collar” improves the field uniformity, as well as the circular polarization and  $B_1^+/B_1^-$  ratio, in and around the neck region. The maximum  $B_1^+$  field

variation in the neck region without the “collar” is  $\delta B_{\max 1} = 61.5\%$  (at approximately  $z = 25$  cm), whereas in the design with the “collar,” it is reduced to  $\delta B_{\max 2} = 22\%$  (at approximately  $z = 30$  cm), which can be observed from Fig. 9.

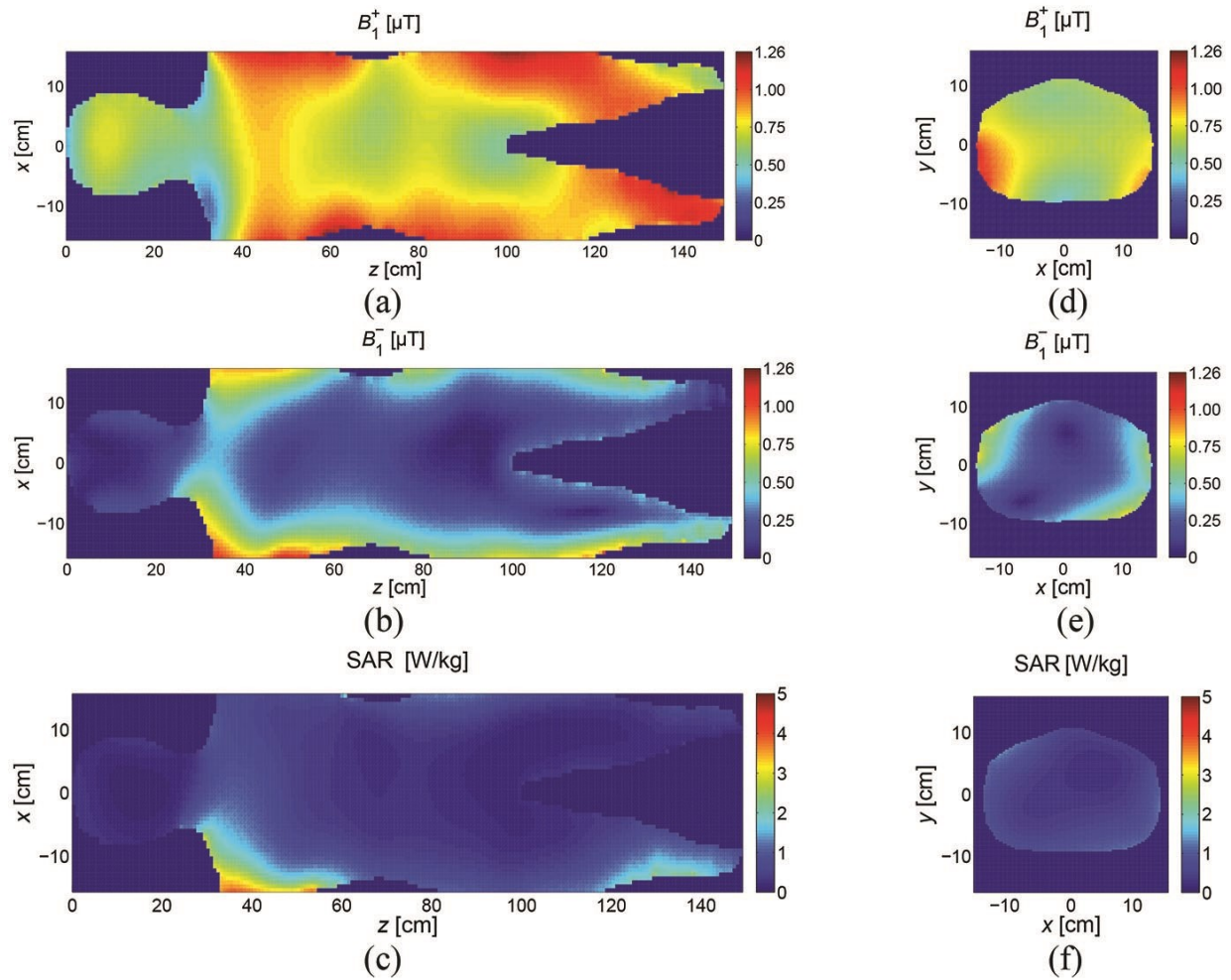


**Fig. 4.9.** 2-D  $B_{1+}$  and  $B_{1-}$  field maps and SAR in (a)–(c) coronal and (d)–(f) axial ( $z = 75$  cm) slices of the human body phantom in Fig. 4.7 with the “collar” in Fig. 4.8.

Fig. 4.9 shows 2-D  $B_{1+}$  and  $B_{1-}$  field maps and SAR in the coronal and axial slices of the human body phantom in Fig. 8 with the “collar” in Fig. 4.8, where we observe a good overall  $B_1$  field uniformity, circular polarization, and SAR levels throughout the phantom.

### 4.3 Dielectric Loading as Dielectric Lenses

Dielectric lenses are added as shown in [66] to the SWGA shown in Fig. 3.3. The dielectric lenses are 5 cm thick, cover the slots completely and are filled with ethylene glycol ( $\epsilon_r = 35$ ).



**Fig. 4.10.** The 3 element slotted waveguide array with dielectric lenses in extendable brackets.

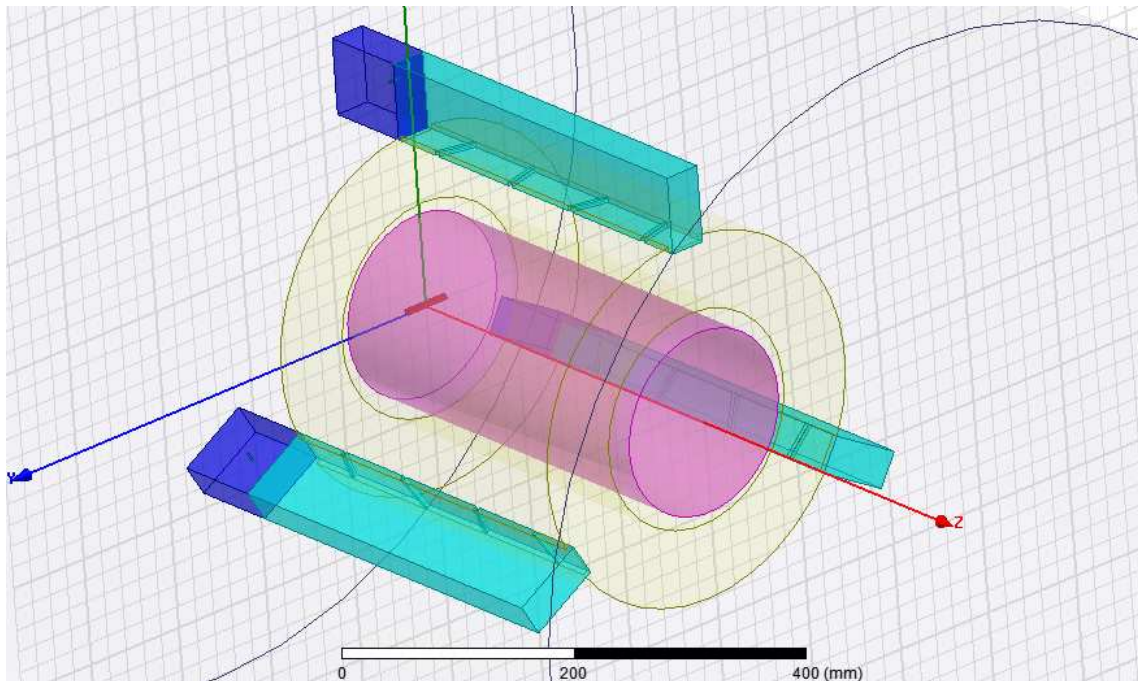


**Fig. 4.11.** HFSS model of the 3 element slotted waveguide array with dielectric lenses around the saline filled cylindrical phantom.

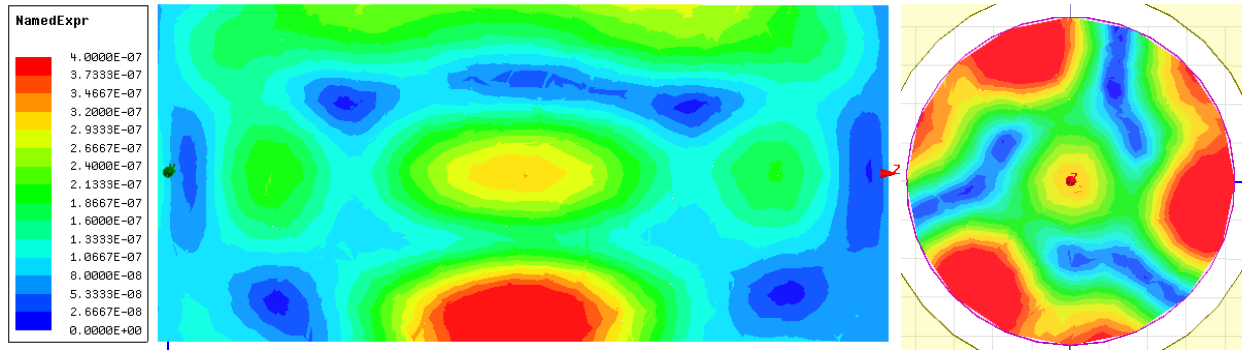


**Fig. 4.12.** Simulated transmit efficiency:  $B_1^+/\sqrt{P_{\text{accepted}}}$  [T/ $\sqrt{W}$ ] inside the phantom in the Coronal and Axial plane, with dielectric lenses.

Comparing Fig. 4.12 to Fig. 3.5, the dielectric lenses greatly increase the transmit efficiency.

## **5 MODELING OF MRI RF COILS USING COMMERCIALY AVAILABLE ELECTROMAGNETIC SOLVERS**

### **5.1 Introduction**

This is based on the paper [70], and addresses application of computational electromagnetics (CEM) to the modeling and full-wave analysis of MRI RF coils for ultra-high field magnetic resonance imaging. RF coil modeling is generally performed using the finite difference-time domain (FD-TD) methods [71]. In this study we explore the possibility of using the method of moments (MoM) in the frequency domain to perform the same analysis.

Here we compare the results obtained from the rigorous full-wave near field computational analysis in the frequency domain based on the MoM using the commercially available software WIPL-D [36] and the finite element method (FEM) using the commercially available software ANSYS HFSS, in the ANSYS Electronics Desktop [37].

### **5.2 FEM and MOM Modeling**

For our simulation models we consider a 7-T MRI system. The MRI bore contains a quadrifilar helical antenna RF coil [31] as the RF exciter with a phantom, as shown in Fig. 5.1.

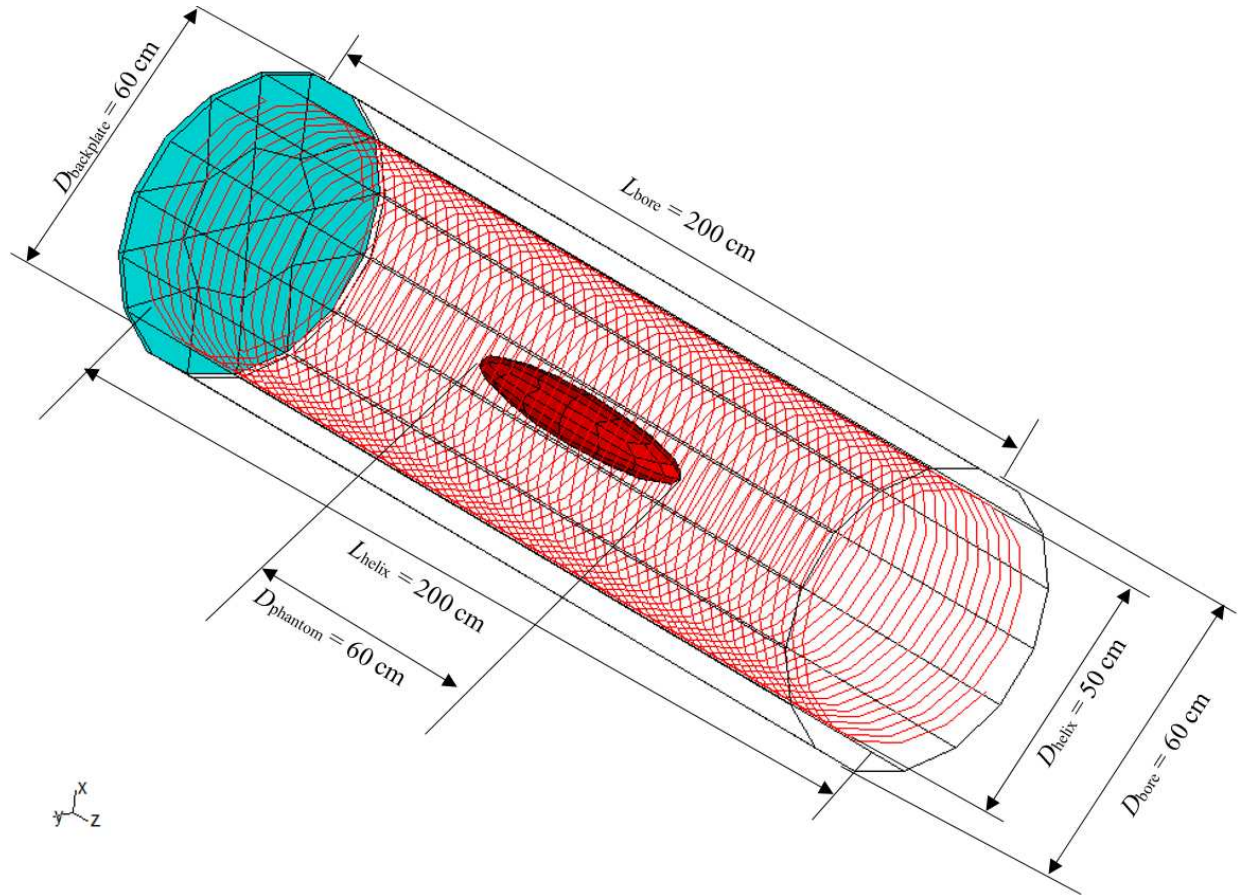


**Fig. 5.1.** WIPL-D model of the quadrifilar helical antenna RF coil with an ellipsoid phantom inside it.

The Larmor frequency for 7-T is 300 MHz. The diameter of the bore considered here is 60 cm and length is 200 cm. A helical antenna is a metallic wire antenna wound periodically with  $N$  wire turns and a pitch  $P$  about an imaginary (or dielectric) cylinder of diameter  $D_{\text{helix}}$  and length  $L_{\text{helix}} = NP$  [35]. The pitch  $P$  relates to the pitch angle,  $\alpha$ , as  $P = C_{\text{helix}} \tan \alpha$ , where  $C_{\text{helix}} = \pi D_{\text{helix}}$  is the helix circumference. The antenna is fed at one wire end against a circular back plate, acting as a ground plane, i.e., the input power is supplied at a lumped excitation port between the wire end and the plate. A quadrifilar helical antenna is an array of four helical antennas connected to the same circular backplate and fed separately. The four helices (channels) are fed in proper phases in order to generate right handed circularly polarized magnetic field along the axis of the helices inside the coil.

The phantom used is a saline-water ( $\epsilon_r = 81$ ,  $\sigma = 0.6$  S/m) filled ellipsoid. Ellipsoid longer axis is 60 cm long and aligned along the axis of the helix and the bore. It is rotationally symmetric and its shorter axis is 10 cm long.

In order to reduce complexity, the four “wire” helices were modeled in ANSYS-HFSS as a thin strips. The width of the strip is chosen as  $a = 4r$ , where  $r = 1$  mm is the radius of the wire in the WIPL-D thin-wire model.

### 5.3 Results and Discussion

In the results we plot and compare  $\mathbf{H}_{\text{rcp}}$ , i.e., the right handed circularly polarized magnetic field and  $\mathbf{H}_{\text{lcp}}$ , i.e., the left handed circularly polarized magnetic field inside the phantom. The aim of the RF coil is to maximize the right handed circularly polarized component of the magnetic field and to minimize the left handed circularly polarized component. Therefore  $\mathbf{H}_{\text{rcp}}$  should be as high as possible and relatively uniform throughout the phantom, whereas  $\mathbf{H}_{\text{lcp}}$  should be minimized and almost 0 on the longer axis of the phantom.

In order to equalize the feed powers in both models the excitation voltage of delta-type generators in the WIPL-D model is scaled to match that of the lumped excitation ports in the ANSYS-HFSS model such that:

$$V_x = \sqrt{\frac{P_{\text{incx}}(1 - |S_{xx}|^2)}{\text{Re}\{Y_{xx}\}}},$$

where  $Y_{xx}$  is input admittance and  $S_{xx}$  is the corresponding  $S$ -parameter for each of the individual helices.

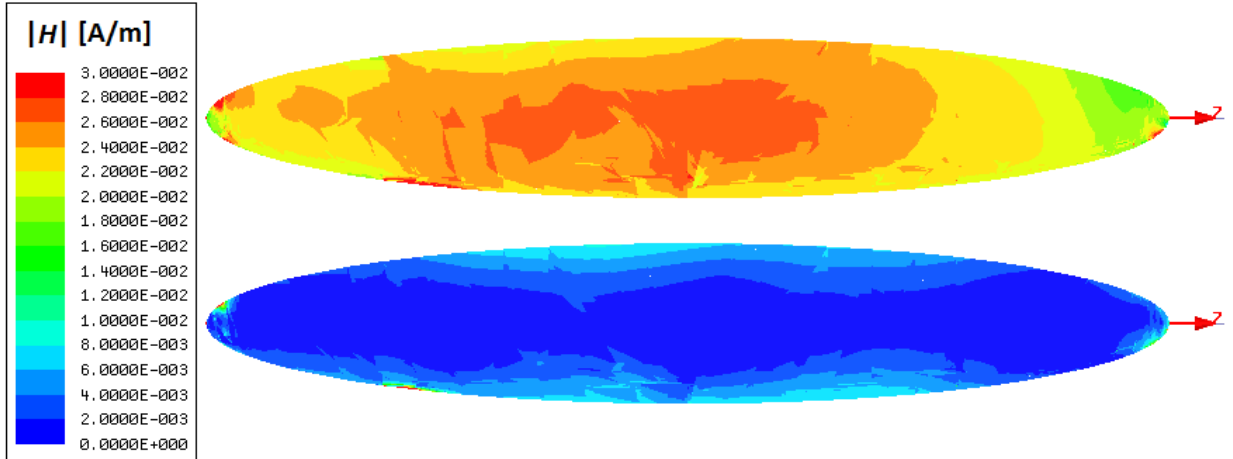


**Fig. 5.2.**  $H_{rep}$  and  $H_{lep}$  in  $xz$ -plane (sagittal/coronal) inside the phantom from ANSYS-HFSS.

The HFSS model run through 7 adaptive passes. Its final mesh comprised 299,584 tetrahedra and the matrix size was 5,394,535 unknowns. Total simulation time was 3 h : 20 m : 38 s. Simulated near field results are shown in Fig. 5.2.

The WIPL-D model had 11,736 unknowns. The order of polynomial expansion on the wires was 2 and on the plates it was a combination of 3 and 4. Total simulation time was 4 m : 24 s. Simulated near field results are shown in Fig. 5.3.

A comparison of  $H_{rep}$  and  $H_{lep}$  on the longer axis of the phantom, i.e., along the  $z$ -axis computed by ANSYS-HFSS and WIPL-D is shown in Fig. 5.4. With a mean deviation of 7.48% in the B1+ field shown in Fig. 5.4. we can conclude that the results are in a very good agreement.

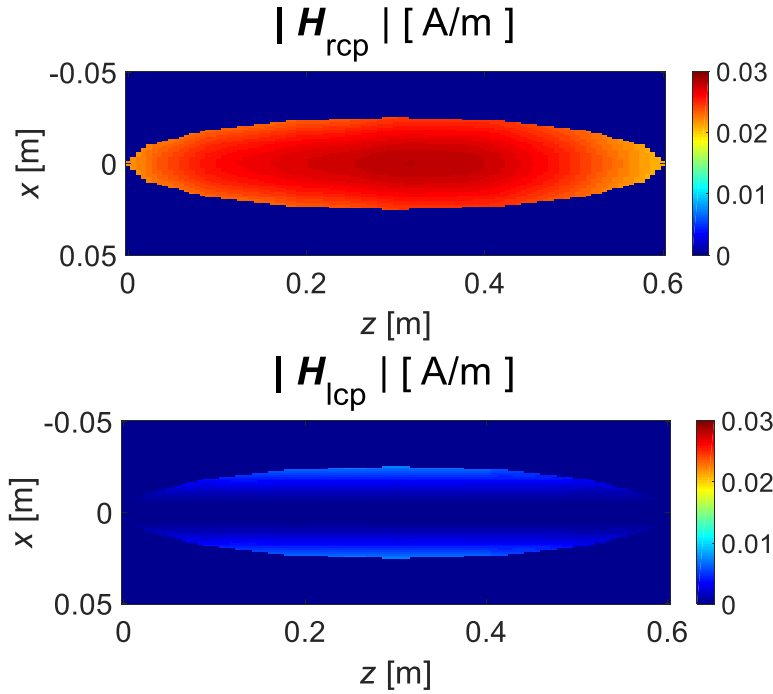


**Fig. 5.3.**  $H_{\text{rcp}}$  and  $H_{\text{lcp}}$  in  $xz$ -plane (sagittal/coronal) inside the phantom from WIPL-D. (Plotted using MATLAB).

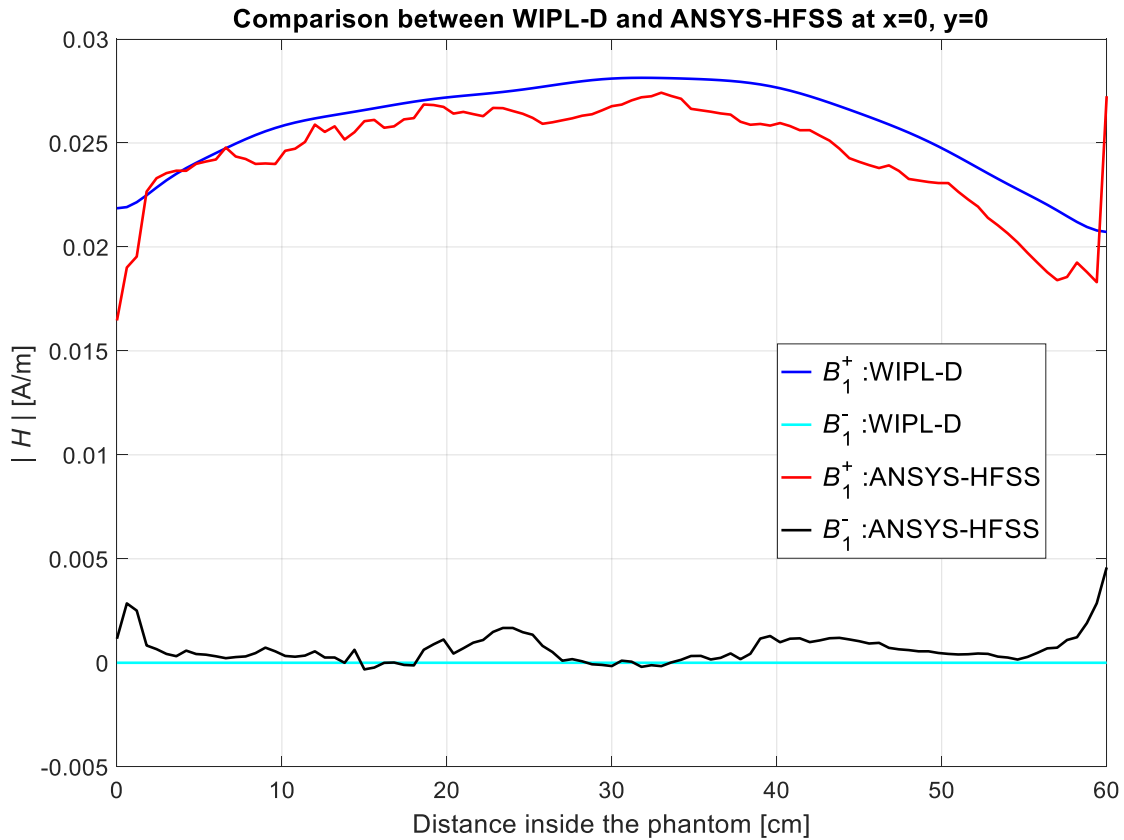


**Fig. 5.4.** Comparison of WIPL-D and ANSYS-HFSS results for  $H_{\text{rcp}}$  and  $H_{\text{lcp}}$  along the  $z$ -axis inside the phantom.

## 6 ONGOING AND FUTURE WORK

### 6.1 Helical Antenna RF Coil for 4.7-T MRI

With the promising results in both 3-T and 7-T, the next task is to design, simulate and experimentally test the concept of multifilar helix for 4.7-T MRI in collaboration with the University of Alberta, Canada, who have a 4.7-T scanner. The Larmor frequency at  $B_0 = 4.7$  T is 200.44 MHz. Instead of focusing on the perfectly cylindrical design, we decided to design and fabricate geometric approximations. These include a rectangular prism and an octagonal prism which effectively mimic a cylinder. This way, the plexiglass frame can be easily constructed to desired dimensions and copper windings can be placed on the antenna body in linear sections between two accurately measured points.

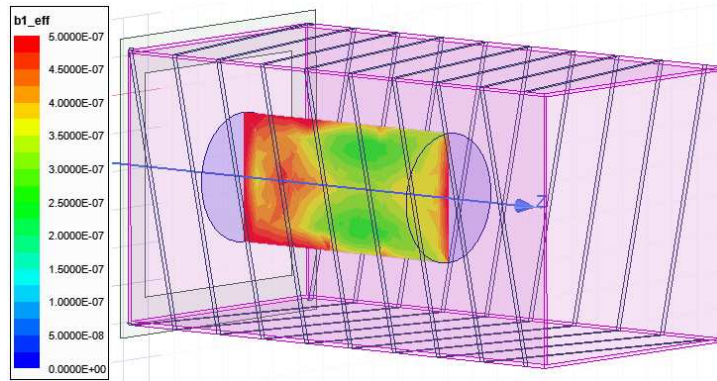


**Fig. 6.1.**  $B_1^+$  efficiency  $[T/\sqrt{W}]$  in sagittal plane inside the cylindrical phantom placed inside the square-prism quadrifilar helical RF coil.

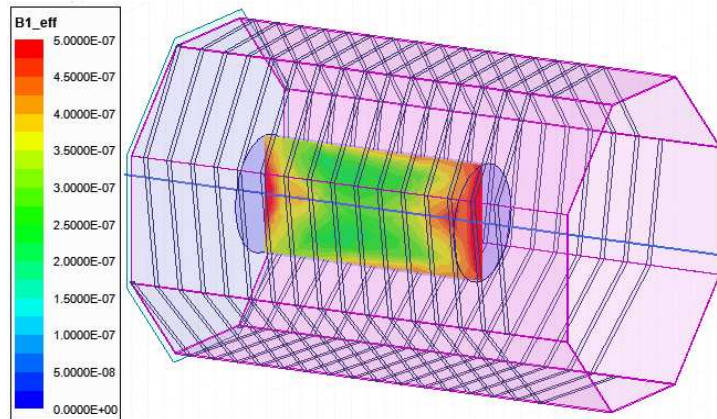


**Fig. 6.2.**  $B_1^+$  efficiency  $[T/\sqrt{W}]$  in sagittal plane inside the cylindrical phantom placed inside the octagonal-prism quadrifilar helical RF coil.

The rectangular prism quadrifilar helical RF coil is 600 mm in length with each side 360 mm and

angle of winding  $12^\circ$  and width of 6 mm. The backplates is 30 mm wider than the helix in the form of a 50 mm ring. The octagonal prism quadrifilar helical RF coil is 588.5 mm in length with each side is 187 mm and angle of winding  $5.7^\circ$  and width of 6 mm. The backplates is 24 mm wider than the helix.

Both design variations were modelled and optimized using FEM simulations in ANSYS-HFSS. The phantoms used in this work are simple homogenous dielectric ( $\epsilon_r = 34$ ,  $\sigma = 0.8$  S/m) cylinders of 170 mm in diameter and 350 mm in length with placed filled along axis of the coil.



**Fig. 6.3.** Square-prism (left) and Octagonal-prism (right) quadrifilar helical RF coil prototypes.

The two prototypes are ready to be experimental with in at the 4.7-T MR scanner facility at the University of Alberta. However, due the unavoidable circumstances due to the COVID-19 pandemic that was put on hold, will be resumed when the situation improves.

## 6.2 Inverted Microstrip Array RF Coil for 7-T MRI

Microstrip transmission lines as microwave exciters have shown to be useful in developing ultra-high-field MRI RF coils [22]. Inverted microstrip line is known to show much favorable characteristics in

practically all aspects than the microstrip line [74-78]. Therefore, we planned to investigate the concept of inverted microstrip array RF coils for MRI.

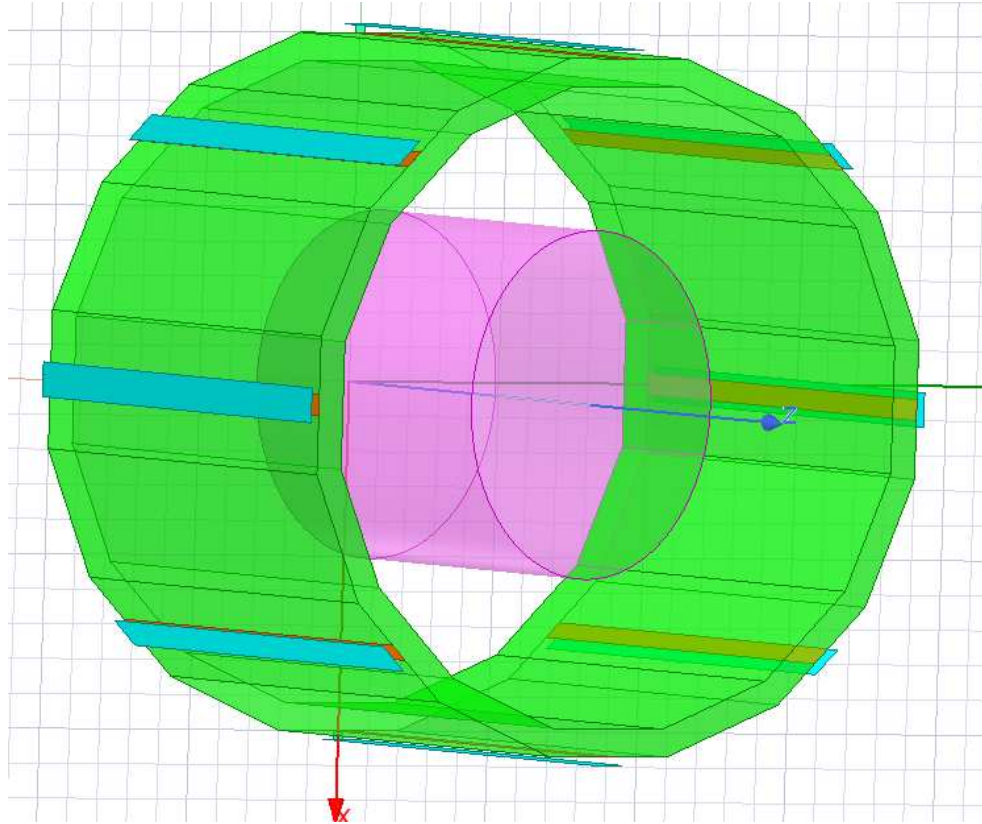


**Fig. 6.3.** ANSYS-HFSS simulation model of the inverted microstrip array RF coil loaded with a saline-filled phantom.

Simulations were performed using ANSYS-HFSS and based on the simulation results, and material availabilities a prototype was built. The distance of the hot-strip of the microstrip lines from the isocenter was kept 20 cm. A saline-filled elliptical-cylindrical phantom of 24 cm length, 10 cm major axis and 8 cm minor axis was simulated. In order to maximize the  $B_1^+$  field efficiency, various dimensional parameters of the coil design were varied. Fig. 6.4 shows two such parameters.

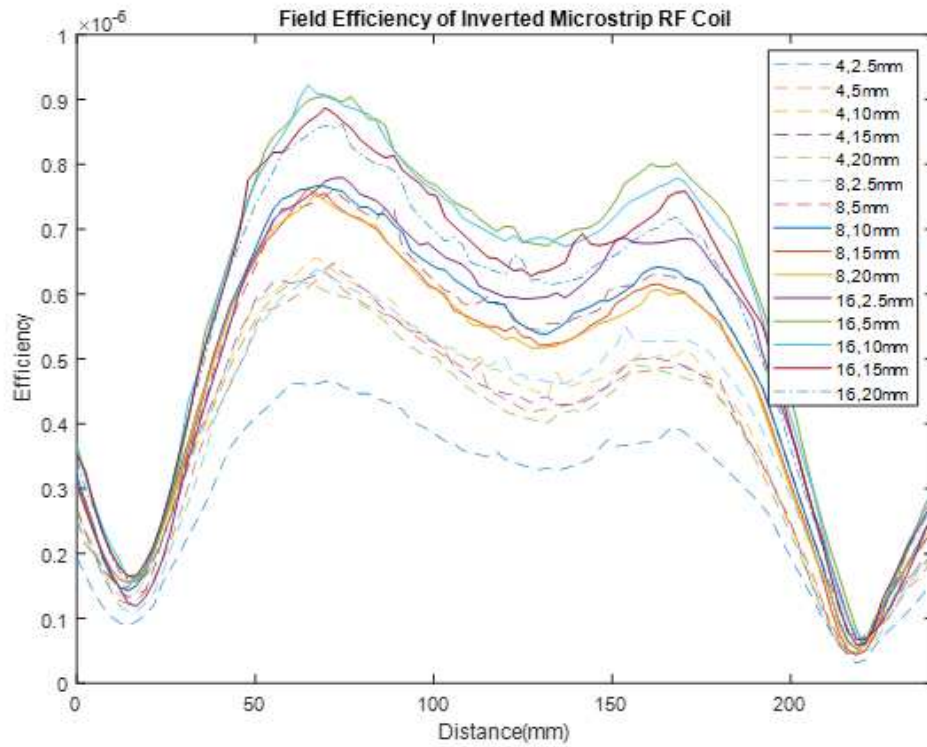


**Fig. 6.4.** Various  $B_1^+$  field efficiency [T/ $\sqrt{W}$ ] simulation results along the longitudinal axis of the phantom for various combinations of dielectric thickness and microstrip-ground separation respectively (shown in the legend).

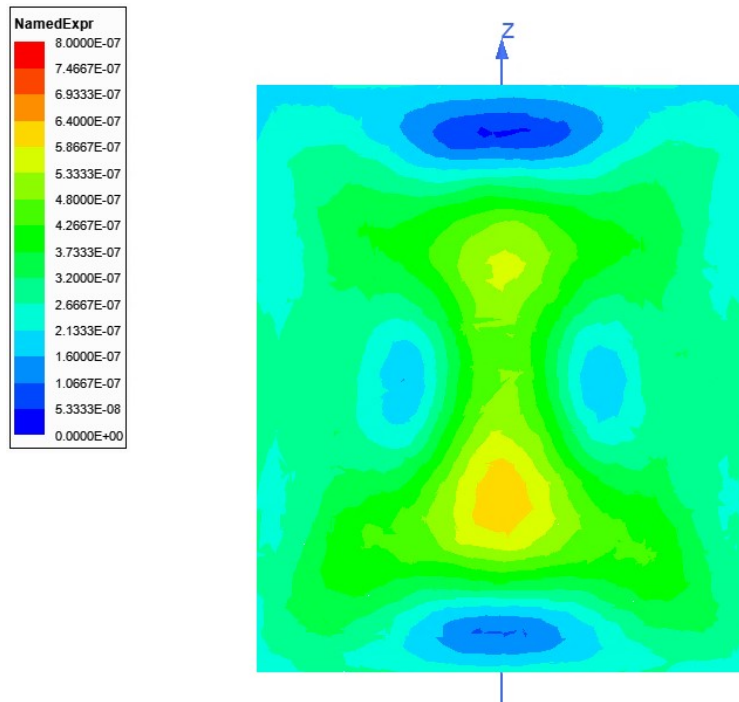


**Fig. 6.5.**  $B_1^+$  field efficiency [T/ $\sqrt{W}$ ] simulation results in the coronal plane of the phantom the coil design with 16 mm thick polyethylene dielectric and 5 mm microstrip-ground plane separation.

Based on simulation models and material availability a prototype was built. The distance of the hot-strip of the microstrip lines from the isocenter was 20 cm, with 16 mm thick polyethylene dielectric and 5 mm microstrip-ground plane separation as can be seen providing optimum field efficiency in Fig. 6.4. and Fig. 6.5. The coil has 8 independent channels and is 30 cm long (shown in Fig. 6.6).

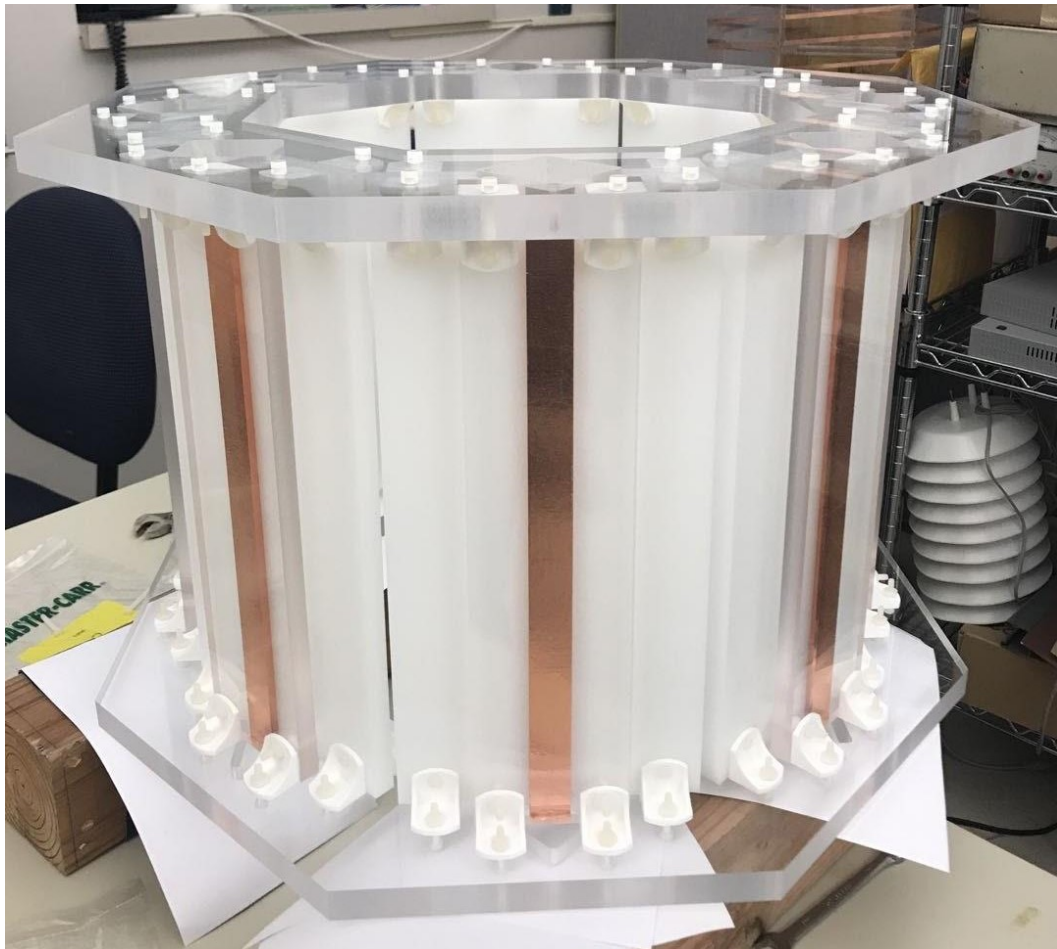


**Fig. 6.6.** Inverted microstrip array RF coil prototype, waiting to be tested in a scanner.

The Inverted Microstrip Array RF Coil prototype is ready to be tested in 7-T MRI scanner. However, due the unavoidable circumstances due to the COVID-19 pandemic that was put on hold, will be resumed when the situation improves.

## REFERENCES

- [1] D. I. Hoult, and P. C. Lauterbur, "Sensitivity of the Zeugmatographic Experiment Involving Human Samples," *J Magn Reson.* 1979;34(2):425-33. doi: Doi 10.1016/0022-2364(79)90019-2. PubMed PMID:WOS:A1979GY24100019.
- [2] P. T. Callaghan, *Principles of Nuclear Magnetic Resonance Microscopy*. New York: Oxford University Press; 1993.
- [3] Z. P. Liang, and P. C. Lauterbur, "Principles of Magnetic Resonance Imaging: A Signal Processing Perspective," New York: IEEE Press; 2000.
- [4] R. W. Brown, Y-C. N. Cheng, E. M. Haacke, R. W. Brown, M. R. Thompson, and Ramesh V., "MRI: Physical Principles and Sequence Design," New York: John Willey & Sons; 1996.
- [5] K. Ugurbil, G. Adriany, P. Andersen, W. Chen, M. Garwood, R. Gruetter, P. G. Henry, S. G. Kim, H. Lieu, I. Tkac, T. Vaughan, P-F. Van De Moortele, E. Yacoub, and X. H. Zhu, "Ultrahigh field magnetic resonance imaging and spectroscopy," *Magnetic Resonance Imaging*, 2003;21(10):1263-81. Epub 2004/01/17. doi: S0730725X03003382 [pii]. PubMed PMID: 14725934.
- [6] K. Ugurbil, "Magnetic resonance imaging at ultrahigh fields," *IEEE Trans Biomed Eng*, 2014;61(5):1364-79. doi: 10.1109/TBME.2014.2313619. PubMed PMID: 24686229; PMCID: PMC4135536.
- [7] J. T. Vaughan, M. Garwood, C. M. Collins, W. Liu, L. DelaBarre, G. Adriany, P. Andersen, H. Merkle, R. Goebel, M. B. Smith, and K. Ugurbil. "7T vs. 4T: RF power, homogeneity, and signal-to-noise comparison in head images," *Magnetic resonance in medicine : official journal of the Society of Magnetic Resonance in Medicine / Society of Magnetic Resonance in Medicine*, 2001;46(1):24-30. Epub 2001/07/10. PubMed PMID: 11443707.
- [8] F. Wiesinger, P-F. Van de Moortele, G. Adriany, N. De Zanche, K. Ugurbil, and K. P. Pruessmann, "Parallel imaging performance as a function of field strength--an experimental investigation using

- electrodynamic scaling,” *Magnetic resonance in medicine : official journal of the Society of Magnetic Resonance in Medicine / Society of Magnetic Resonance in Medicine*, 2004;52(5):953-64. Epub 2004/10/28. doi: 10.1002/mrm.20281. PubMed PMID: 15508167.
- [9] F. Wiesinger, P-F. Van de Moortele, G. Adriany, N. De Zanche, K. Ugurbil, and K. P. Pruessmann, “Potential and feasibility of parallel MRI at high field,” *NMR in Biomedicine*, 2006;19(3):368-78. doi: 10.1002/nbm.1050. PubMed PMID: WOS:000238086200009.
- [10] D. I. Hoult, and D. Phil. “Sensitivity and power deposition in a high-field imaging experiment,” *J Magn Reson Imaging*, 2000;12(1):46-67. PubMed PMID: 10931564.
- [11] E. Moser, F. Stahlberg, and M. E. Ladd, and S. Trattnig, “7-T MR--from research to clinical applications?” *NMR Biomed*, 2012;25(5):695-716. doi: 10.1002/nbm.1794. PubMed PMID: 22102481.
- [12] A. G. Webb, and P-F. Van de Moortele, “The technological future of 7 T MRI hardware,” *NMR Biomed*, 2015. doi: 10.1002/nbm.3315. PubMed PMID: 25974894.
- [13] X. Wu, J. T. Vaughan, K. Ugurbil, and P-F. Van de Moortele, “Parallel Excitation in the Human Brain at 9.4 T Counteracting k-Space Errors With RF Pulse Design,” *Magnetic resonance in medicine: official journal of the Society of Magnetic Resonance in Medicine / Society of Magnetic Resonance in Medicine*, 2010;63(2):524-9. Epub 2009/12/18. doi: 10.1002/mrm.22247. PubMed PMID: 20017161; PMCID: 3066148.
- [14] J. Budde, G. Shajan, M. Zaitsev, K. Scheffler, and R. Pohmann, “Functional MRI in human subjects with gradient-echo and spin-echo EPI at 9.4 T,” *Magn Reson Med*, 2014;71(1):209-18. doi: 10.1002/mrm.24656. PubMed PMID: 23447097.
- [15] X. Wu, G. Adriany, K. Ugurbil, and P-F. Van de Moortele, “Parallel Transmission in Human Brain at 9.4T Counteracting Eddy Current Induced Excitation Errors in RF Pulse Design,” *Proc Intl Soc Mag Reson Med*, 2011;19:4441.

- [16] J. Budde, G. Shajan, J. Hoffmann, K. Ugurbil, and R. Pohmann, "Human imaging at 9.4 T using T(2)\*-, phase-, and susceptibility-weighted contrast," *Magn Reson Med*, 2011;65(2):544-50. doi: 10.1002/mrm.22632. PubMed PMID: 20872858.
- [17] U. Katscher, P. Bornert, C. Leussler, and J. S. van den Brink, "Transmit SENSE," *Magn Reson Med*. 2003;49(1):144-50. PubMed PMID: 12509830.
- [18] Y. Zhu, "Parallel excitation with an array of transmit coils," *Magn Reson Med*, 2004;51(4):775-84. PubMed PMID: 15065251.
- [19] H. P. Hetherington, N. I. Avdievich, A. M. Kuznetsov, and J. W. Pan, "RF shimming for spectroscopic localization in the human brain at 7 T," *Magn Reson Med*, 2010;63(1):9-19. PubMed PMID: 19918903.
- [20] K. Setsompop, L. L. Wald, V. Alagappan, B. Gagoski, F. Hebrank, U. Fontius, F. Schmitt, and E. Adalsteinsson, "Parallel RF transmission with eight channels at 3 Tesla," *Magn Reson Med*, 2006;56(5):1163-71. PubMed PMID: 17036289.
- [21] G. J. Metzger, C. Snyder, C. Akgun, T. Vaughan, K. Ugurbil, and P-F. Van de Moortele, "Local B1+ shimming for prostate imaging with transceiver arrays at 7T based on subject-dependent transmit phase measurements," *Magn Reson Med*, 2008;59(2):396-409. Epub 2008/01/30. doi: 10.1002/mrm.21476. PubMed PMID: 18228604.
- [22] G. Adriany, P-F. Van de Moortele, F. Wiesinger, S. Moeller, J. P. Strupp, P. Andersen, C. Snyder, X. Zhang, W. Chen, K. P. Pruessmann, P. Boesiger, T. Vaughan, and K. Ugurbil, "Transmit and receive transmission line arrays for 7 Tesla parallel imaging" *Magn Reson Med*. 2005;53(2):434-45. Epub 2005/01/29. doi: 10.1002/mrm.20321. PubMed PMID: 15678527.
- [23] J. T. Vaughan, L. DelaBarre, C. Snyder, J. Tian, P. Andersen, J. Strupp, G. Adriany, P-F. Van de Moortele, and K. Ugurbil, editors, "9.4T Human Imaging: Preliminary Results," *Proc Intl Soc Mag Reson Med*, 2006 May; Seattle.

- [24] J. T. Vaughan, C. J. Snyder, L. J. DelaBarre, P. J. Bolan, J. Tian, L. Bolinger, G. Adriany, P. Andersen, J. Strupp, and K. Ugurbil, "Whole-body imaging at 7T: preliminary results," *Magn Reson Med*, 2009;61(1):244-8. PubMed PMID: 19097214.
- [25] G. J. Metzger, P-F. van de Moortele, C. Akgun, C. J. Snyder, S. Moeller, J. Strupp, P. Andersen, D. Shrivastava, T. Vaughan, K. Ugurbil, and G. Adriany, "Performance of External and Internal Coil Configurations for Prostate Investigations at 7 T," *Magnetic resonance in medicine : official journal of the Society of Magnetic Resonance in Medicine / Society of Magnetic Resonance in Medicine*, 2010;64(6):1625-39. doi: 10.1002/mrm.22552. PubMed PMID: WOS:000284659300011.
- [26] G. J. Metzger, E. J. Auerbach, C. Akgun, J. Simonson, X. Bi, K. Ugurbil, and P-F. van de Moortele, "Dynamically applied B1+ shimming solutions for non-contrast enhanced renal angiography at 7.0 Tesla," *Magn Reson Med*, 2013;69(1):114-26. Epub 2012/03/24. doi: 10.1002/mrm.24237. PubMed PMID: 22442056; PMCID: 3387512.
- [27] A. J. Raaijmakers, P. R. Luijten, and C. A. van den Berg, "Dipole antennas for ultrahigh-field body imaging: a comparison with loop coils," *NMR Biomed*, 2015. doi: 10.1002/nbm.3356. PubMed PMID: 26278544.
- [28] H. Barfuss, H. Fischer, D. Hentschel, R. Ladebeck, and J. Vetter, "Whole-body MR imaging and spectroscopy with a 4-T system," *Radiology*, 1988;169(3):811-6. doi: 10.1148/radiology.169.3.3187004. PubMed PMID: 3187004.
- [29] C. M. Collins, S. Li, and M. B. Smith, "SAR and B1 field distributions in a heterogeneous human head model within a birdcage coil. Specific energy absorption rate," *Magn Reson Med*, 1998;40(6):847-56. PubMed PMID: 9840829.
- [30] C. M. Collins, and M. B. Smith "Signal-to-noise ratio and absorbed power as functions of main magnetic field strength, and definition of "90 degrees " RF pulse for the head in the birdcage coil," *Magn Reson Med*, 2001;45(4):684-91. PubMed PMID: 11283997.

- [31] P. S. Athalye, N. J. Sekeljić, M. M. Ilić, A. A. Tonyushkin, B. M. Notaroš, "Subject-loaded quadrifilar helical-antenna RF coil with high B<sub>1+</sub> field uniformity and large FOV for 3-T MRI" *Concepts in Magnetic Resonance Part B – Magnetic Resonance Engineering*, 2016, doi: 10.1002/cmr.b.21326.
- [32] S.J. Eustace, E. Nelson, "Whole body magnetic resonance imaging; A valuable adjunct to clinical examination". *BMJ : British Medical Journal*, 2004; 328(7453):1387–1388.
- [33] B. M. Notaros, "Higher order frequency-domain computational electromagnetics". Invited review paper, Special Issue on Large and Multiscale Computational Electromagnetics, *IEEE Trans Antennas Propagat*, 2008; 56:2251–2276.
- [34] M. Djordjevic, B. M. Notaros, "Double higher order method of moments for surface integral equation modeling of metallic and dielectric antennas and scatterers". *IEEE Trans Antennas Propagat*, 2004; 52:2118–2129.
- [35] A. R. Djordjević, A. G. Zajić, M. M. Ilić, G. Stuber, "Optimization of helical antennas". [Antenna Designer's Notebook] *IEEE Antennas Propagat Magazine*, 2006; 48:107–115.
- [36] WIPL-D Pro v11, WIPL-D d.o.o. 2014. Available: <http://www.wipl-d.com>.
- [37] HFSS, ANSYS® Electromagnetics Suite 15.0.7, ANSYS, Inc. Available: <http://www.ansys.com>.
- [38] M. A. Ohliger, D. K. Sodickson, "An introduction to coil array design for parallel MRI". *NMR Biomed*, 2006; 19:300–315.
- [39] A. Andreychenko, H. Kroeze, D. W. Klomp, J. J. Lagendijk, P. R. Luijten, C. A. van den Berg, "Coaxial waveguide for travelling wave MRI at ultrahigh fields". *Magn Reson Med*, 2013; 70:875–884.
- [40] W. M. Brink, M. J. Versluis, J. M. Peeters, P. Börnert, A.G. Webb, "Passive Radiofrequency Shimming in the Thigh at 3 Tesla using High Permittivity Material and Body Coil Receive Uniformity Correction". *Magn Reson Med*, 2015; Version of Record online.

- [41] R. Brown, K. Lakshmanan, G. Madelin, L. Alon, G. Chang, D. K. Sodickson, R. R. Regatte, G. C. Wiggins, "A flexible Nested Sodium and Proton Coil Array with Wideband Matching for Knee Cartilage MRI at 3T". *Magn Reson Med*, 2015 [Epub ahead of print].
- [42] B. Guérin, M. Gebhardt, P. Serano, E. Adalsteinsson, M. Hamm, J. Pfeuffer, J. Nistler, L. L. Wald, "Comparison of Simulated Parallel Transmit Body Arrays at 3 T Using Excitation Uniformity, Global SAR, Local SAR, and Power Efficient Metrics". *Magn Reson Med*, 2015; 73:1137–1150.
- [43] R. Pohmann, O. Speck, K. Scheffler, "Signal-to-Noise Ratio and MR Tissue Parameters in Human Brain Imaging at 3,4, and 9.4 Tesla Using Current Receive Coil Arrays". *Magn Reson Med*, 2015; 75:801–809.
- [44] J. Hoffmann, G. Shajan, J. Budde, K. Scheffler, R. Pohmann, "Human Brain Imaging at 9.4 T using a Tunable Patch Antenna for Transmission". *Magn Reson Med*, 2013; 69:1494–1500.
- [45] D. O. Brunner, J. Paška, J. Froehlich, K. P. Pruessmann, "Traveling-Wave RF Shimming and Parallel MRI". *Magn Reson Med*, 2011; 66:290–300.
- [46] A. Andreychenko, H. Kroeze, V. O. Boer, J. J. Lagendijk, P. R. Luijten, C. A. van den Berg, "Improved steering of the RF field of traveling wave MR with a multimode, coaxial waveguide". *Magn Reson Med*, 2014; 71: 1641–1649.
- [47] B. Zhang, D. K. Sodickson, R. Lattanzi, Q. Duan, B. Stoeckel, G. C. Wiggins, "Whole Body Traveling Wave Magnetic Resonance Imaging at High Field Strength: Homogeneity, Efficiency, and Energy Deposition as Compared with Traditional Excitation Mechanisms". *Magn Reson Med*, 2013; 67:1183–1193.
- [48] B. M. Notaros, "Electromagnetics" *New Jersey: PEARSON Prentice Hall*; 2010.
- [49] M. M. Ilić, I. Perović, A. A. Tonyushkin, P. Athalye, N. Škeljić, B. M. Notaroš, "Full-wave frequency-domain electromagnetic modelling of RF fields in MRI applications". In: *Proceedings of the 2015 IEEE International Symposium on Antennas and Propagation, Vancouver, BC, Canada, July 19-25 2015*; pp 971–972.

- [50] M. Alecci, C. M. Collins, M. B. Smith, P. Jezzard, "Radio frequency magnetic field mapping of a 3 T birdcage coil: experimental and theoretical dependence on sample properties". *Magn Reson Med*, 2001; 46:379–385.
- [51] M. Alecci, C. M. Collins, J. Wilson, W. Liu, M. B. Smith, P. Jezzard, "Theoretical and experimental evaluation of detached endcaps for 3 T birdcage coils". *Magn Reson Med*, 2003; 49:363–370.
- [52] F. Vazquez, R. Martin, O. Marrufo, A. O. Rodriguez, "Travelling wave magnetic resonance imaging at 3T". *J Appl Phys*, 2013 [Online] 114:064906. Available: <http://dx.doi.org/10.1063/1.4817972>.
- [53] F. Vazquez, R. Martin, O. Marrufo, A. O. Rodriguez, "Travelling wave magnetic resonance imaging at 3 Tesla". *Medical Physics*, 2013 [arXiv: 1301.3426v1].
- [54] A. Kangarlu, B. A. Baertlein, R. Lee, T. Ibrahim, L. Yang, A. M. Abduljalil, P. M. Robitaille, "Dielectric resonance phenomena in ultra high field MRI". *J Comput Assist Tomogr*. 1999;23(6):821-31. PubMed PMID: 10589554.
- [55] H. Bomsdorf, T. Helzel, D. Kunz, P. Roschmann, O. Tschendel, J. Wieland, "Spectroscopy and imaging with a 4 tesla whole-body MR system". *NMR Biomed*, 1988;1(3):151-8. PubMed PMID: 3275125.
- [56] C. M. Collins, M. B. Smith. "Signal-to-noise ratio and absorbed power as functions of main magnetic field strength, and definition of "90 degrees " RF pulse for the head in the birdcage coil". *Magn Reson Med*. 2001;45(4):684-91. PubMed PMID: 11283997.
- [57] D. I. Hoult, "The principle of reciprocity in signal strength calculations - A mathematical guide" *Concepts in Magnetic Resonance*, 2000;12(4):173-87. doi: 10.1002/1099-0534(2000)12:4<173::Aid-Cmr1>3.0.Co;2-Q. PubMed PMID: WOS:000087677000001.
- [58] C. E. Hayes, W. A. Edelstein, J. F. Schenck, O. M. Mueller, M Eash, "An Efficient, Highly Homogeneous Radiofrequency Coil for Whole-Body NMR Imaging at 1.5-T". *Journal of Magnetic Resonance*. 1985;63(3):622-8. doi: Doi 10.1016/0022-2364(85)90257-4. PubMed PMID: WOS:A1985ANE0500024.

- [59] D. C. Alsop, T. J. Connick, G. Mizsei, "A spiral volume coil for improved RF field homogeneity at high static magnetic field strength". *Magn Reson Med.* 1998;40(1):49-54. PubMed PMID: 9660552.
- [60] P. S. Athalye, M. M. Ilić, P.-F. van de Moortele, A. J. M. Kiruluta, B. M. Notaroš, "Multi-channel helical-antenna inner-volume RF coils for ultra-high field MR scanners", *Concepts in Magnetic Resonance Part B – Magnetic Resonance Engineering*, 2018, doi: 10.1002/cmr.b.21405.
- [61] D. J. Kraus, "Helical beam antennas", *Electronics* 1947;20:109–11.
- [62] D. J. Kraus, "Antennas", *New York: McGraw-Hill*; 1988.
- [63] D. J. Lee, P. M. Glover, editors. "A Comparison of a Patch Antenna to an End-fire Helix Antenna for use in Travelling Wave MRI". *Proc of the Joint Annual Meeting ISMRM-ESMRMB 2010*; 2010; Stockholm.
- [64] A. J. E. Raaijmakers, A. Van der Werf, H. Kroeze, P. R. Lujten, C. A. T. Van den Berg, D. W. J. Klomp, "Helix antennas: approaching the target from a different angle". *Proc of the Joint Annual Meeting ISMRM-ESMRMB 2014*, Milan, Italy. 201.
- [65] S.-M.Sohn, L. BelaBarre, G. Anand, J. T. Vaughan, "RF Head Coil Design With Improved RF Magnetic Near-Fields Uniformity for Magnetic Resonance Imaging (MRI) Systems". *Magnetic Resonance in Medicine*, 2014; 71:1641-1649(2014). doi:10.1109/TMTT.2014.2331621.
- [66] M. M. Ilić, B. M. Notaroš, "Slotted-waveguide array radio frequency for ultra-high-field magnetic resonance imaging", *Concepts in Magnetic Resonance Part B – Magnetic Resonance Engineering*, 2018, doi: 10.1002/cmr.b.21367.
- [67] C. A. Balanis, "Modern Antenna Handbook:" *A John Wiley & Sons*; 2008.
- [68] D. O. Brunner, N. De Zanche, J. Frohlich, J. Paska, K. P. Pruessmann, "Travelling-wave nuclear magnetic resonance". *Nature*, 2009;457(7232):994-8. PubMed PMID: 19225521.
- [69] A. Tonyushkin, N. B. Konyer, L. M. Ranzani, Z. Popovich, M. D. Noseworthy, A. J. M. Kiruluta, "Improvement of traveling wave performance at 3T using high dielectric rods", *In: Proceedings of the 55th Experimental Nuclear Magnetic Resonance Conf.*, Pacific Grove, California, USA, 2014.

- [70] P. S. Athalye, B. M. Notaroš, M. M. Ilić, "Full-wave modelling of RF exciters using WIPL-D: Road to real-time simulation and optimization" *ACES Journal*, 2018; Vol. 33, No. 10.
- [71] H. Yoo, A. Gopinath, and J. T. Vaughan, "A method to localize RF  $B_1$  field in high-field magnetic resonance imaging systems," *IEEE Trans. on Biomedical Engineering*, vol. 59, Dec. 2012, pp. 3365-3371.
- [72] C. A. Van den Berg, B. Van den Bergen, J. B. Van de Kamer, B. W. Raaymakers, H. Kroeze, L. W. Bartels, J. J. Lagendijk, "Simultaneous  $B_+$  homogenization and specific absorption rate hotspot suppression using a magnetic resonance phased array transmit coil". *Magn Reson Med*, 2007; 57:577–586.
- [73] Q. X. Yang, S. Rupprecht, W. Luo, C. Sica, Z. Herse, J. Wang, Z. Cao, J. Vesek, M. T. Lanagan, G. Carluccio, Y. C. Ryu, C. M. Collins, "Radiofrequency field enhancement with high dielectric constant (HDC) pads in a receive array coil at 3.0 T". *J Magn Reson Imag*, 2013; 38: 435–440.
- [74] B. E. Spielman, "Dissipation loss effects in isolated and coupled transmission lines". *IEEE Trans on Microwave Theory and Techniques*, 1977; 25 (8): 646–656.
- [75] R. S. Tomar, P. Bhatia, "New quasi-static models for the computer-aided design of suspended and inverted microstrip lines" (short paper). *IEEE Trans on Microwave Theory and Techniques*, 1987; 35: 453–457.
- [76] R. S. Tomar, P. Bhatia, "New dispersion models for open suspended substrate microstrips". *IEEE Trans on Microwave Theory and Techniques*, 1988 25–27 May 1988. p 387–389 vol.381.
- [77] J. Liu, J. Yang, A. U. Zaman, " Study of Dielectric Loss and Conductor Loss among Microstrip, covered Microstrip and inverted Microstrip Gap Waveguide utilizing variational Method in Millimeter Waves ". *International Symposium on Antenna and Propagation*, 2018 23–26 Oct 2018. p 1–2.
- [78] G. E. Ponchak, M. M. Tentzeris, "Multiple modes on embedded inverted microstrip lines". *Topical meeting on silicon monolithic integrated circuits in RF systems*, 2006; 23–26 Oct 2006. P 1–2.

## PUBLICATIONS

M. M. Ilić, A. A. Tonyushkin, P. S. Athalye, N. J. Šekeljić, A. J. M. Kiruluta, and B. M. Notaroš, "RF magnetic field profiling with a dielectric bore lining for traveling waves in a 3-T MRI scanner: a computational study", *ACES Journal*, 2020; Vol. 35, No. 3, pp. 245-249, 2020

P. S. Athalye, B. M. Notaroš, M. M. Ilić, "Full-wave modelling of RF exciters using WIPL-D: Road to real-time simulation and optimization" *ACES Journal*, 2018; Vol. 33, No. 10.

P. S. Athalye, M. M. Ilić, P-F van de Moortele, A. J. M. Kiruluta, B. M. Notaroš, "Multi-channel helical-antenna inner-volume RF coils for ultra-high field MR scanners", *Concepts in Magnetic Resonance Part B – Magnetic Resonance Engineering*, 2018, doi: 10.1002/cmr.b.21405.

P. S. Athalye, N. J. Sekeljić, M. M. Ilić, A. A. Tonyushkin, B. M. Notaroš, "Subject-loaded quadrifilar helical-antenna RF coil with high B<sub>1+</sub> field uniformity and large FOV for 3-T MRI" *Concepts in Magnetic Resonance Part B – Magnetic Resonance Engineering*, 2016, doi: 10.1002/cmr.b.21326.

P. S. Athalye, M. M. Ilić, P-F Van de Moortele, A. J. M. Kiruluta, B. M. Notaroš, "Multi-Channel Helical-Antenna Inner-Volume RF Coils for Ultra-High-Field MR Scanners". (Abstract) *Proceedings of the 24th Scientific Meeting of the International Society for Magnetic Resonance in Medicine, ISMRM 2016*, 7-13 May 2016, Singapore. 2016.

P. S. Athalye, N. J. Šekeljić, M. M. Ilić, A. A. Tonyushkin, A. J. M. Kiruluta, P-F Van de Moortele, B. M. Notaroš, "Long and Short Monofilar and Quadrifilar Helical Antenna RF Coils at 7 T". (Abstract) *Invited Presentation. 10th Biennial 2015 Minnesota Workshop on High and Ultra-High Field Imaging*, October 1-3, 2015, Minneapolis, MN. 2015

M. M. Ilić, I. Perović, A. A. Tonyushkin, P. Athalye, N. Šekeljčić, B. M. Notaroš, "Full-wave frequency-domain electromagnetic modelling of RF fields in MRI applications". In: *Proceedings of the 2015 IEEE International Symposium on Antennas and Propagation, Vancouver, BC, Canada, July 19-25 2015*; pp 971–972.

B. M. Notaroš, M. M. Ilić, A. A. Tonyushkin, N. J. Sekeljčić, P. Athalye, "Quadrifilar Helical Antenna as a Whole-Body Traveling-Wave RF Coil for 3T and 7T MRI". (Abstract) *Proceedings of the 23th Scientific Meeting of the International Society for Magnetic Resonance in Medicine, ISMRM 2015, 30 May - 5 June, 2015, Toronto, Ontario, Canada*. p.1825. 2015.

M. M. Ilić, A. A. Tonyushkin, N. Šekeljčić, P. Athalye, B. M. Notaroš, "RF excitation in 7 tesla MRI systems using monifilar axial-mode helical antenna", *2015 IEEE International Symposium on Antennas and Propagation & USNC/URSI National Radio Science Meeting, 2015*; doi: 10.1109/APS.2015.7305062

P. Athalye, N. J. Šekeljčić, M. M. Ilić, A. A. Tonyushkin, B. M. Notaroš, "Improving traveling-wave RF field inside magnetic resonance imaging bores by incorporating dielectric loadings", *2015 USNC-URSI Radio Science Meeting (Joint with AP-S Symposium), 2015*; doi: 10.1109/USNC-URSI.2015.7303600